Semi-analytical solution for the 3D response of a tunnel embedded in an elastic half-space subject to seismic waves

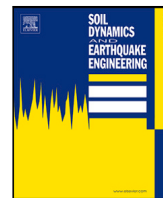Zhao, Mingjuan; de Oliveira Barbosa, João Manuel; Metrikine, Andrei V.; van Dalen, Karel N.

Important note
To cite this publication, please use the final published version (if applicable).
Please check the document version above.

Semi-analytical solution for the 3D response of a tunnel embedded in an elastic half-space subject to seismic waves

Mingjuan Zhao [*], João Manuel de Oliveira Barbosa, Andrei V. Metrikine, Karel N. van Dalen

Faculty of Civil Engineering and Geosciences, Delft University of Technology, Stevinweg 1, 2628 CN, Delft, The Netherlands

ARTICLE INFO

ABSTRACT

This paper presents a semi-analytical solution for the 3D problem of a cylindrical tunnel embedded in an elastic half-space subject to plane harmonic compressional and shear waves. Both the tunnel and soil are modelled as an elastic continuum. Conformal mapping is employed to transform the original physical domain with boundary surfaces of two different types onto an image domain with surfaces of the same type, which makes the problem easier to solve. The total wave field in the half-space consists of incident and reflected (from the half-space surface) plane waves, as well as directly and secondary scattered cylindrical waves, while the total wave field in the tunnel consists of refracted cylindrical waves. The secondary scattered waves, generated when the cylindrical waves directly scattered from the tunnel meet the half-space surface, are represented by cylindrical waves that originate from an image source, which is in line with the spirit of the method of images. The unknown amplitude coefficients of the cylindrical waves are determined from the boundary and continuity conditions of the tunnel–soil system by projecting those onto the set of circumferential modes, which results in a set of algebraic equations. Results show that the present method converges for a small number of circumferential modes. We observe very good agreement between the obtained results and those in literature. In a systematic evaluation, we demonstrate that the method works well for the frequency band of seismic waves, as well as for the complete considered ranges of the tunnel/soil stiffness ratio, the embedded depth of the tunnel, the vertical incident angle and the tunnel thickness. However, the results obtained for a moderate tunnel–soil stiffness contrast under the incident compressional wave are inaccurate when Hankel functions are used to represent the cylindrical waves in the tunnel, which is due to the refracted shear waves in the tunnel transitioning from propagating to evanescent (in the 3D case). These inaccuracies can be perfectly overcome by representing the waves in the tunnel by Bessel functions. We also find that the present method generally works better for the incident compressional wave than for the incident shear wave, as the condition number of the matrix (related to the mentioned algebraic equations) is often larger in the latter case. In view of engineering practice, we conclude that the tunnel is safer when the surrounding soil is stiffer, the tunnel is thicker and the vertical incident angle is larger. Finally, the present method, which is in general fast, elegant and accurate, can be used in preliminary design so as to avoid pronounced resonances, and to assess stress distributions and ground vibrations.

1. Introduction

Underground tunnels and pipelines are important infrastructures due to numerous applications in civil engineering. The dynamics of these underground structures subject to dynamic loadings, such as seismic waves or moving trains, have been studied by many researchers in the past [1–4].

The ground is often modelled by a half-space, which consists of an infinite domain beneath a flat stress-free surface. The challenges in solving the boundary value problem of a cylindrical tunnel embedded in a half-space are as follows: (1) The half-space domain is infinite, and it is often computationally expensive and challenging to satisfy the boundary conditions at large distance when applying numerical methods [5]; (2) The boundary surfaces are of two different types (i.e. flat and cylindrical), and it is difficult to deal with this issue especially when applying analytical methods; (3) It can be very difficult to get accurate results due to ill-conditioned matrices encountered for specific solution methods [6].

The existing approaches to study the scattering of waves by underground structures can be divided into two categories: analytical methods and numerical methods. These two types of methods have

their own pros and cons. Analytical methods are computationally efficient but can only deal with structures of simple geometries. Numerical methods, on the other hand, can handle structures of complex geometries but are often computationally expensive because of the large domains that need to be discretised. The most often used numerical methods are Finite Element Methods (FEM), Finite Difference Methods (FDM), Boundary Element Methods (BEM) and combinations of those. A comprehensive overview of the features of these different methods applied to the problem of wave scattering by underground structures in a half-space can be found in [5].

With the development of more powerful computers, numerical methods have been widely applied to investigate the dynamic amplifications induced by the scattering of plane waves by underground structures and canyons at the ground surface. For example, Luco and de Barros [6–10] employed the indirect BEM to examine the 2D or 3D responses of infinitely long cylindrical inclusions embedded in a layered poroelastic half-space. A simplified Donnell shell theory was used to model pipelines. The applications of the indirect BEM to other wave scattering problems can be found in the work by Dravinski and Mossessian [11]. The advantage of the indirect BEM is that (integrable) singularities of the Green's functions are eliminated by locating the source positions away from the integral surface at which the observation positions are located. A special direct BEM was used by Stamos and Beskos [5,12] to determine the 3D dynamic response of underground structures in a half-space. In their paper, quadratic isoparametric boundary line elements and an advanced numerical integration technique for the treatment of singular integrals were used to produce results of high accuracy. Furthermore, the combination of BEM and FEM was applied by Liu et al. [13] to study the 3D response of pipelines buried in a half-space. The above mentioned methods are all frequency-domain based. Some work conducted in the time domain employing FEM or BEM can be found in Refs. [14–18]. Note that the BEM is often more efficient compared to other numerical methods, as explicit expressions for the employed Green's functions are available (in the frequency–wavenumber domain), and only surfaces need to be discretised. Therefore, the BEM can also be perceived as semi-analytical method.

Analytical methods are usually based on wave-function expansions. Using the method of separation of variables, wave functions satisfying the wave or Helmholtz equations in Cartesian or cylindrical coordinates, respectively, are obtained. The unknown coefficients in the wave-function expansions (i.e., general solutions) can be determined based on boundary conditions. Wave functions were first used by Pao and Mow [1] to study the wave scattering from a cavity in a full-space. To solve the unknown coefficients for more complicated problems involving a half-space, additional techniques need to be employed. For the 2D SH wave scattering problem in a half-space with an embedded tunnel, the method of images was used to obtain a closed-form steady-state solution [19]. The P-SV problem in a half-space is more complicated to solve due to mode conversions between the P and SV waves at the half-space surface and at the tunnel. To tackle this, Datta and EL-Akily [20–22] employed a method of matched asymptotic expansions and a method of successive reflections to calculate the response of the considered half-space system. Lee and Zhu [23] employed Legendre polynomials to represent both P and S wave functions so that zero-stress boundary conditions at the half-space surface can be satisfied. Other examples of analytical solutions to solve the wave scattering problems can be found in Refs. [24,25].

To circumvent the difficulty arising due to the two different bounding surfaces in the problem of cylindrical structures embedded in a half-space, Cao and Lee [26], and Lee and Karl [27] proposed to approximate the flat half-space boundary by an almost flat circular boundary of a large radius. The aim of the current study is to present a semi-analytical solution without employing this approximation. To cope with the challenge of the two different boundary surfaces, the method of conformal mapping (which employs the complex-variable
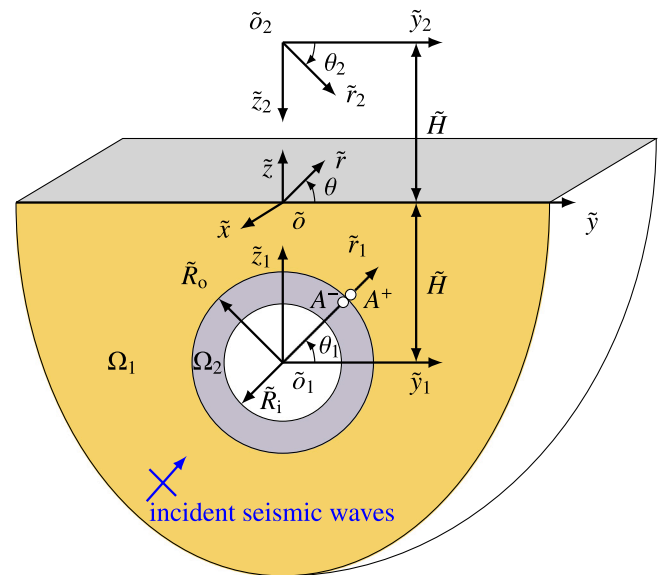

Fig. 1. A 3D model of a tunnel embedded in an elastic half-space subjected to seismic waves and the employed coordinate systems.

theory) can be used; it transforms a domain with flat and cylindrical boundary surfaces into a domain with cylindrical surfaces only [28]. Liu et al. [29] were the first to apply the method of conformal mapping to solve the 2D full-space wave scattering by a cavity problem. Then, Verruijt [30] also used this method to solve the problem of a circular cavity in an elastic half-space with prescribed static loads acting on the cavity surface. Later on, the method was used by Liu et al. to solve the 2D problem of two closely-spaced circular cavities subject to plane harmonic waves in a full-space [31], and to solve the 2D dynamic problem of a tunnel embedded in an elastic half-space subjected to seismic waves [32]. The current paper aims to extend the method to the 3D case, and present a systematic evaluation of the performance of the method, which is lacking in the other studies.

This paper is organised as follows. In Section 2, we present the statement of the considered problem. Section 3 presents incident and reflected plane-wave fields in the soil, and scattered and refracted cylindrical-wave fields in the soil and tunnel, respectively. Stress and displacement expressions in terms of complex variables are given in Section 4. The conformal mapping functions are introduced in Section 5. In Section 6, we determine the unknown coefficients of potentials related to the cylindrical waves. After having solved the problem, convergence tests and validations of the proposed method are given in Section 7. Furthermore, an evaluation of the accuracy of the present method is given in Section 8. The accuracy is analysed for varying dimensionless frequency, the stiffness ratio of the tunnel to soil, the embedded depth of the tunnel, the vertical incident angle and the thickness of the tunnel. The effects of these five important factors on the response of the system are briefly addressed as well. Finally, Section 9 presents the conclusions.

2. Problem statement

In this paper, we consider the three-dimensional model shown in Fig. 1. An infinitely long tunnel embedded in an elastic half-space is subjected to seismic waves with the wave propagation direction being arbitrary. The tunnel has a circular cross-section, and the longitudinal axis of the tunnel is parallel to the half-space surface. Both the tunnel and the half-space are modelled as an elastic continuum which is assumed isotropic and linearly elastic.

Regions Ω_1 and Ω_2 shown in Fig. 1 refer to the domains of the soil and tunnel, respectively. For the analysis, it is convenient to
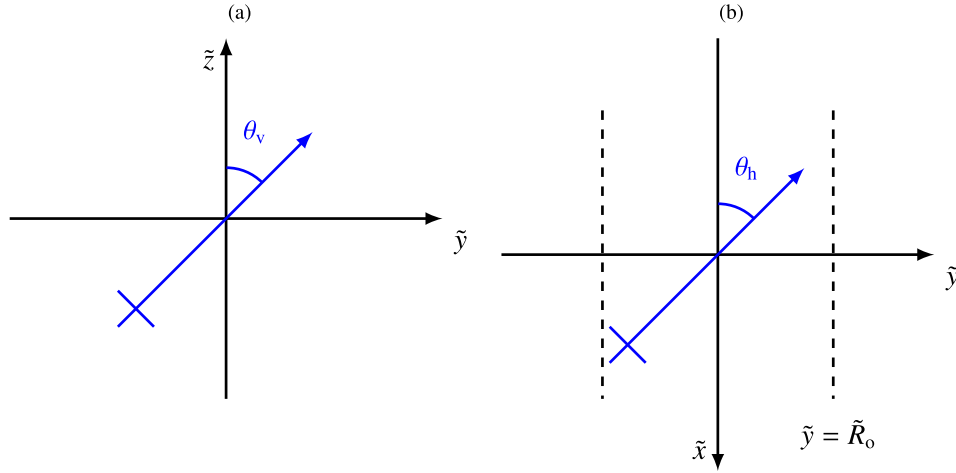
Fig. 2. Incident angles: (a) vertical incident angle and (b) horizontal incident angle.

use six coordinate systems: global Cartesian $(\tilde{y}, \tilde{z}, \tilde{x})$ and cylindrical $(\tilde{r}, \theta, \tilde{x})$ coordinates with origin at the free surface of the half-space, local Cartesian $(\tilde{y}_1, \tilde{z}_1, \tilde{x}_1)$ and cylindrical $(\tilde{r}_1, \theta_1, \tilde{x}_1)$ coordinates with origin at the centre of the tunnel, and local Cartesian $(\tilde{y}_2, \tilde{z}_2, \tilde{x}_2)$ and cylindrical $(\tilde{r}_2, \theta_2, \tilde{x}_2)$ coordinates with origin at the centre of the image of the tunnel. The centre of the tunnel $\tilde{o}_1$ is located beneath the free surface at a depth of $\tilde{H}$, and the inner and outer radii of the tunnel are denoted as $\tilde{R}_i$ and $\tilde{R}_o$, respectively. The image of the tunnel is symmetrically positioned with respect to the free surface. As shown in Fig. 2, the vertical incident angle θ_v is defined as the angle between the wave propagation direction and the positive vertical $\tilde{z}$ axis, while the horizontal incident angle θ_h is the angle between the projection of the wave propagation direction on the horizontal plane (i.e., $(\tilde{x}, \tilde{y})$-plane) and the negative $\tilde{x}$ axis. Throughout this paper, a tilde is used to denote that parameters, coordinates, variables and operators are dimensional.

2.1. Governing equations and boundary conditions

As we are interested in the steady-state solution to the problem, we assume that both the excitations and the responses of the system are harmonic and proportional to $e^{+i\tilde{\omega}\tilde{t}}$, where i is the imaginary unit, $\tilde{t}$ time, $\tilde{\omega} = 2\pi\tilde{f}$ the angular frequency and $\tilde{f}$ the frequency in Hz. In what follows, the factor $e^{+i\tilde{\omega}\tilde{t}}$ is left out from all the expressions for brevity. The governing equations of motion of the soil medium and the tunnel in the frequency domain, without external forces, read [2,3]:

$$\left(\tilde{\lambda}^{(i)} + \tilde{\mu}^{(i)}\right)\tilde{\nabla}\tilde{\nabla}\cdot\tilde{\mathbf{u}}^{(i)} + \tilde{\mu}^{(i)}\tilde{\nabla}^2\tilde{\mathbf{u}}^{(i)} = -\tilde{\omega}^2\tilde{\rho}^{(i)}\tilde{\mathbf{u}}^{(i)}, \tag{1}$$

where $\tilde{\lambda}^{(i)}$ and $\tilde{\mu}^{(i)}$ signify the Lamé constants, and $\tilde{\rho}^{(i)}$ the material density; the superscript $i = \{1, 2\}$ indicates the soil or tunnel, respectively; $\tilde{\nabla}$ is the three-dimensional gradient vector (for Cartesian coordinates, as an example, $\tilde{\nabla} = (\partial_{\tilde{y}}, \partial_{\tilde{z}}, \partial_{\tilde{x}})$), $\tilde{\nabla}^2$ is the Laplace operator (e.g., $\tilde{\nabla}^2 = \partial_{\tilde{y}}^2 + \partial_{\tilde{z}}^2 + \partial_{\tilde{x}}^2$), and $\tilde{\mathbf{u}}^{(i)}$ is a displacement vector (e.g., $\tilde{\mathbf{u}}^{(i)} = (\tilde{u}_{\tilde{y}}^{(i)}, \tilde{u}_{\tilde{z}}^{(i)}, \tilde{u}_{\tilde{x}}^{(i)})$).

The excitations of the system are seismic waves coming from below the tunnel. Therefore, we have stress-free boundary conditions at both the free surface of the half-space and the inner surface of the tunnel. We assume that the soil and tunnel are perfectly bonded, which implies that we have continuity conditions at the tunnel–soil interface. Accordingly, these stress-free boundary and continuity conditions are written as follows:

$$
\begin{aligned}
\tilde{\sigma}_{\tilde{z}\tilde{z}}^{(1)} = \tilde{\sigma}_{\tilde{z}\tilde{y}}^{(1)} = \tilde{\sigma}_{\tilde{z}\tilde{x}}^{(1)} = 0, & \qquad \tilde{z} = 0, \\
\tilde{\sigma}_{\tilde{r}_1\tilde{r}_1}^{(2)} = \tilde{\sigma}_{\tilde{r}_1\theta_1}^{(2)} = \tilde{\sigma}_{\tilde{r}_1\tilde{x}_1}^{(2)} = 0, & \qquad \tilde{r}_1 = \tilde{R}_i, \\
\tilde{u}_{\tilde{r}_1}^{(1)} = \tilde{u}_{\tilde{r}_1}^{(2)}, \quad \tilde{u}_{\theta_1}^{(1)} = \tilde{u}_{\theta_1}^{(2)}, \quad \tilde{u}_{\tilde{x}_1}^{(1)} = \tilde{u}_{\tilde{x}_1}^{(2)}, & \qquad \tilde{r}_1 = \tilde{R}_o, \\
\tilde{\sigma}_{\tilde{r}_1\tilde{r}_1}^{(1)} = \tilde{\sigma}_{\tilde{r}_1\tilde{r}_1}^{(2)}, \tilde{\sigma}_{\tilde{r}_1\theta_1}^{(1)} = \tilde{\sigma}_{\tilde{r}_1\theta_1}^{(2)}, \tilde{\sigma}_{\tilde{r}_1\tilde{x}_1}^{(1)} = \tilde{\sigma}_{\tilde{r}_1\tilde{x}_1}^{(2)}, & \qquad \tilde{r}_1 = \tilde{R}_o.
\end{aligned} \tag{2}
$$

2.2. Application of the Helmholtz decomposition

It is noted that the displacement components in Eq. (1) are coupled. For ease of finding solutions, we apply the Helmholtz decomposition $\tilde{\mathbf{u}}^{(i)} = \tilde{\nabla}\tilde{\phi}^{(i)} + \tilde{\nabla} \times \tilde{\mathbf{\Psi}}^{(i)}$, which reduces the elastodynamic equation of motion to two uncoupled Helmholtz equations:

$$\tilde{\nabla}^2\tilde{\phi}^{(i)} + \left(\tilde{k}_P^{(i)}\right)^2\tilde{\phi}^{(i)} = 0, \tag{3}$$

$$\tilde{\nabla}^2\tilde{\mathbf{\Psi}}^{(i)} + \left(\tilde{k}_S^{(i)}\right)^2\tilde{\mathbf{\Psi}}^{(i)} = 0, \tag{4}$$

where Eq. (3) is a scalar potential equation, and Eq. (4) is a vector potential equation; $\tilde{\phi}^{(i)}$ and $\tilde{\mathbf{\Psi}}^{(i)}$ are potentials related to dilatational and rotational motions, respectively; $\tilde{k}_P^{(i)} = \tilde{\omega}/\tilde{c}_P^{(i)}$ and $\tilde{k}_S^{(i)} = \tilde{\omega}/\tilde{c}_S^{(i)}$ are the compressional and shear wavenumbers; $\tilde{c}_P^{(i)} = \sqrt{(\tilde{\lambda}^{(i)} + 2\tilde{\mu}^{(i)})/\tilde{\rho}^{(i)}}$ and $\tilde{c}_S^{(i)} = \sqrt{\tilde{\mu}^{(i)}/\tilde{\rho}^{(i)}}$ are the propagation velocities of the compressional and shear waves.

The vector potential $\tilde{\mathbf{\Psi}}^{(i)}$ needs to satisfy the gauge condition $\tilde{\nabla} \cdot \tilde{\mathbf{\Psi}}^{(i)} = 0$, so that only two of the three components of $\tilde{\mathbf{\Psi}}^{(i)}$ are independent. We split up the vector potential $\tilde{\mathbf{\Psi}}^{(i)}$ as follows [3,33]:

$$
\begin{aligned}
\tilde{\mathbf{\Psi}}^{(i)} &= \tilde{\mathbf{\Psi}}_1^{(i)} + \tilde{\mathbf{\Psi}}_2^{(i)}, \\
\tilde{\mathbf{\Psi}}_1^{(i)} &= \tilde{\psi}^{(i)}\mathbf{e}_{\tilde{x}} + \left(\tilde{k}_S^{(i)}\right)^{-2}\tilde{\nabla}\left(\frac{\partial\tilde{\psi}^{(i)}}{\partial\tilde{x}}\right), \\
\tilde{\mathbf{\Psi}}_2^{(i)} &= \left(\tilde{k}_S^{(i)}\right)^{-1}\tilde{\nabla} \times \left(\tilde{\chi}^{(i)}\mathbf{e}_{\tilde{x}}\right),
\end{aligned} \tag{5}
$$

in which $\mathbf{e}_{\tilde{x}}$ is the unit vector along $\tilde{x}$ axis. The vector potential $\tilde{\mathbf{\Psi}}_1^{(i)}$ is defined such that the associated particle motion is polarised only in the vertical plane (i.e., $(\tilde{y}, \tilde{z})$-plane); the other vector potential $\tilde{\mathbf{\Psi}}_2^{(i)}$ is defined such that the associated particle motion is polarised in all directions. This can be observed in the displacement expressions in Section 2.3 (see Eq. (10), contributions of $\psi^{(i)}$ and $\chi^{(i)}$).

By defining the vector potentials as in Eq. (5), the equation for the vector potential, Eq. (4), can be reduced to two uncoupled scalar potential equations:

$$
\begin{aligned}
\tilde{\nabla}^2\tilde{\psi}^{(i)} + \left(\tilde{k}_S^{(i)}\right)^2\tilde{\psi}^{(i)} &= 0, \\
\tilde{\nabla}^2\tilde{\chi}^{(i)} + \left(\tilde{k}_S^{(i)}\right)^2\tilde{\chi}^{(i)} &= 0.
\end{aligned} \tag{6}
$$

2.3. Non-dimensionalisation

For the analysis of the problem, we introduce non-dimensional parameters, coordinates, variables and operators. These are defined as

$$\{x, y, z, x_1, y_1, z_1, x_2, y_2, z_2, r, r_1, r_2\}$$
$$= \{\tilde{x}, \tilde{y}, \tilde{z}, \tilde{x}_1, \tilde{y}_1, \tilde{z}_1, \tilde{x}_2, \tilde{y}_2, \tilde{z}_2, \tilde{r}, \tilde{r}_1, \tilde{r}_2\}\Big/\tilde{H},$$

$$\{H, R_i, R_o, \mathbf{u}^{(i)}\} = \{\tilde{H}, \tilde{R}_i, \tilde{R}_o, \tilde{\mathbf{u}}^{(i)}\}\Big/\tilde{H},$$

$$\{c_P^{(i)}, c_S^{(i)}\} = \{\tilde{c}_P^{(i)}, \tilde{c}_S^{(i)}\}\Big/\tilde{c}_S^{(1)}, \quad t = \tilde{t}\tilde{c}_S^{(1)}\Big/\tilde{H}, \quad \omega = \tilde{\omega}\tilde{H}\Big/\left(\pi\tilde{c}_S^{(1)}\right),$$

$$\{k_P^{(i)}, k_S^{(i)}\} = \{\tilde{k}_P^{(i)}, \tilde{k}_S^{(i)}\}\tilde{H}, \quad \{\phi^{(i)}, \psi^{(i)}, \chi^{(i)}\} = \{\tilde{\phi}^{(i)}, \tilde{\psi}^{(i)}, \tilde{\chi}^{(i)}\}\Big/\tilde{H}^2,$$

$$\{\lambda^{(i)}, \mu^{(i)}\} = \{\tilde{\lambda}^{(i)}, \tilde{\mu}^{(i)}\}\Big/\tilde{\mu}^{(1)}, \quad \rho^{(i)} = \tilde{\rho}^{(i)}\left(\tilde{c}_S^{(1)}\right)^2\Big/\tilde{\mu}^{(1)}. \tag{7}$$

Accordingly, the dimensionless Helmholtz equations are obtained as

$$\nabla^2 \phi^{(i)} + \left(k_P^{(i)}\right)^2 \phi^{(i)} = 0,$$

$$\nabla^2 \psi^{(i)} + \left(k_S^{(i)}\right)^2 \psi^{(i)} = 0, \tag{8}$$

$$\nabla^2 \chi^{(i)} + \left(k_S^{(i)}\right)^2 \chi^{(i)} = 0.$$

The boundary and continuity conditions (see Eq. (2)) of the problem in terms of dimensionless variables and parameters are as follows:

$$\begin{aligned}
\sigma_{zz}^{(1)} = \sigma_{zy}^{(1)} = \sigma_{zx}^{(1)} &= 0, & z &= 0, \\
\sigma_{r_1 r_1}^{(2)} = \sigma_{r_1 \theta_1}^{(2)} = \sigma_{r_1 x_1}^{(2)} &= 0, & r_1 &= R_i, \\
u_{r_1}^{(1)} = u_{r_1}^{(2)}, \quad u_{\theta_1}^{(1)} = u_{\theta_1}^{(2)}, \quad u_{x_1}^{(1)} &= u_{x_1}^{(2)}, & r_1 &= R_o, \\
\sigma_{r_1 r_1}^{(1)} = \sigma_{r_1 r_1}^{(2)}, \sigma_{r_1 \theta_1}^{(1)} = \sigma_{r_1 \theta_1}^{(2)}, \sigma_{r_1 x_1}^{(1)} &= \sigma_{r_1 x_1}^{(2)}, & r_1 &= R_o.
\end{aligned} \tag{9}$$

Based on the dimensionless Helmholtz decomposition $\mathbf{u}^{(i)} = \nabla \phi^{(i)} + \nabla \times \mathbf{\Psi}^{(i)}$ and the definition of the vector potential (see Eq. (5)), the displacement components can be expressed in terms of the three dimensionless scalar potentials $\phi^{(i)}$, $\psi^{(i)}$ and $\chi^{(i)}$:

$$u_y^{(i)} = \frac{\partial \phi^{(i)}}{\partial y} + \frac{\partial \psi^{(i)}}{\partial z} + \frac{1}{k_S^{(i)}}\frac{\partial^2 \chi^{(i)}}{\partial x \partial y},$$

$$u_z^{(i)} = \frac{\partial \phi^{(i)}}{\partial z} - \frac{\partial \psi^{(i)}}{\partial y} + \frac{1}{k_S^{(i)}}\frac{\partial^2 \chi^{(i)}}{\partial x \partial z}, \tag{10}$$

$$u_x^{(i)} = \frac{\partial \phi^{(i)}}{\partial x} + \frac{1}{k_S^{(i)}}\left(\left(k_S^{(i)}\right)^2 \chi^{(i)} + \frac{\partial^2 \chi^{(i)}}{\partial x^2}\right).$$

The 3D problem is reduced to a 2D one by letting $\partial/\partial x = 0$ (i.e., $k_x^{(1)} = 0$, $k_x^{(1)}$ is introduced later, in Eq. (13)), corresponding to the case when $\theta_h = 90°$ or $\theta_v = 0°$. From the displacement expressions shown in Eq. (10), we observe that the scalar potential $\psi^{(i)}$ in the 2D case is related to the well-known SV wave because $\psi^{(i)}$ only contributes to motions ($u_y^{(i)}$ and $u_z^{(i)}$) in the vertical plane (y, z); on the contrary, the other scalar potential $\chi^{(i)}$ is related to the SH wave because $\chi^{(i)}$ only contributes to the horizontally polarised out-of-plane motion $u_x^{(i)}$. Therefore, the 3D problem is reduced to decoupled 2D plane-strain (P-SV) and 2D anti-plane (SH) problems when $\partial/\partial x = 0$. However, in the 3D case, we cannot uniquely relate the potentials $\psi^{(i)}$ and $\chi^{(i)}$ to SV and SH waves, respectively, although $\psi^{(i)}$ still only contributes to motions in the (y, z)-plane for the 3D case (while the associated wave generally propagates in all directions).

The Cartesian stress components in terms of potentials can be easily obtained using the well-known Hooke's law [4]. The cylindrical displacement and stress components in terms of potentials could be derived in a similar way as demonstrated above (i.e., derived in Cartesian coordinates; see Eq. (10)). To do that, one would need to consider the gradient vector, the Laplace operator and the displacement vector in cylindrical coordinates (i.e., $\nabla = \left(\partial_r, (1/r)\partial_\theta, \partial_x\right)^T$, $\nabla^2 = \partial_r^2 + (1/r)\partial_r + \left(1/r^2\right)\partial_\theta^2 + \partial_x^2$, $\mathbf{u}^{(i)} = \left(u_r^{(i)}, u_\theta^{(i)}, u_x^{(i)}\right)^T$) instead of those in

Cartesian coordinates shown in Section 2.1. As an alternative, we derive the cylindrical displacement and stress expressions by transforming the ones in Cartesian coordinates using the following relations for the displacement vector $\mathbf{u}$ and stress tensor σ, respectively:

$$\begin{bmatrix} u_r \\ u_\theta \\ u_x \end{bmatrix} = \mathbf{T}\begin{bmatrix} u_y \\ u_z \\ u_x \end{bmatrix}, \quad \mathbf{T} = \begin{bmatrix} \cos(\theta) & \sin(\theta) & 0 \\ -\sin(\theta) & \cos(\theta) & 0 \\ 0 & 0 & 1 \end{bmatrix}, \tag{11}$$

$$\begin{bmatrix} \sigma_{rr} & \sigma_{r\theta} & \sigma_{rx} \\ \sigma_{\theta r} & \sigma_{\theta\theta} & \sigma_{\theta x} \\ \sigma_{xr} & \sigma_{x\theta} & \sigma_{xx} \end{bmatrix} = \mathbf{T}\begin{bmatrix} \sigma_{yy} & \sigma_{yz} & \sigma_{yx} \\ \sigma_{zy} & \sigma_{zz} & \sigma_{zx} \\ \sigma_{xy} & \sigma_{xz} & \sigma_{xx} \end{bmatrix}\mathbf{T}^T, \tag{12}$$

where the superscript "(i)" is omitted for brevity, the cylindrical coordinate system (r, θ, x) is defined based on $y = r\cos(\theta)$ and $z = r\sin(\theta)$, $\mathbf{T}$ is the transformation matrix, and $\mathbf{T}^T$ is its transpose.

3. Solutions of the governing equations

In this section, we aim to solve the governing equations specified in Eq. (8). These Helmholtz equations can be solved using the method of separation of variables in the Cartesian and cylindrical coordinate systems separately [33]. The solutions are used to construct the complete wave field in the system [4].

3.1. Incident and reflected plane waves

Our ultimate goal is to solve the dynamic problem shown in Fig. 1. As the problem of interest is linear, we first consider a submodel which is a half-space without a tunnel, subject to seismic excitations, and find the wave field in the half-space based on the stress-free boundary conditions at the free surface. Then, we add the embedded tunnel in the half-space, and find the additional wave field due to the presence of the tunnel; for this model the excitation is the response calculated in the previous submodel at the factitious tunnel–soil interface. The sum of the two wave fields obtained in both models form the total wave field.

Thus, considering first a half-space without the underground structure, we have harmonic plane waves as the solutions to Eq. (8). Reflected waves are generated when the incident wave meets the free surface of the half-space, and propagate away from the free surface. The sum of the incident and reflected plane waves form the wave field in the half-space. Three cases will be discussed in this subsection: incident compressional ($\phi_{inc}^{(1)}$) and shear ($\psi_{inc}^{(1)}$ and $\chi_{inc}^{(1)}$) waves, where the subscript "inc" indicates the incident wave.

Case 1: Incident compressional wave. The plane-wave solutions for the incident ($\phi_{inc}^{(1)}$) and reflected waves ($\phi_{ref}^{(1)}$, $\psi_{ref}^{(1)}$, $\chi_{ref}^{(1)}$) are given as

$$\phi_{inc}^{(1)} = \phi_0 \exp\left(-i k_x^{(1)} x - i k_y^{(1)} y - i k_{z,P}^{(1)} z\right),$$

$$\phi_{ref}^{(1)} = R_{\phi,\phi}\phi_0 \exp\left(-i k_x^{(1)} x - i k_y^{(1)} y + i k_{z,P}^{(1)} z\right),$$

$$\psi_{ref}^{(1)} = R_{\psi,\phi}\phi_0 \exp\left(-i k_x^{(1)} x - i k_y^{(1)} y + i k_{z,S}^{(1)} z\right), \tag{13}$$

$$\chi_{ref}^{(1)} = R_{\chi,\phi}\phi_0 \exp\left(-i k_x^{(1)} x - i k_y^{(1)} y + i k_{z,S}^{(1)} z\right),$$

where the subscript "ref" indicates the reflected wave; ϕ_0 is the amplitude of the incident compressional wave, $R_{\phi,\phi}$, $R_{\psi,\phi}$ and $R_{\chi,\phi}$ (given in Appendix A) are amplitude ratios of the reflected waves $\phi_{ref}^{(1)}$, $\psi_{ref}^{(1)}$ and $\chi_{ref}^{(1)}$, to the incident compressional wave $\phi_{inc}^{(1)}$, respectively. The wavenumbers $k_x^{(1)}$ and $k_y^{(1)}$ in the x and y directions are written as

$$k_x^{(1)} = k_{x,P}^{(1)} = -k_P^{(1)} \sin(\theta_v)\cos(\theta_h), \quad k_y^{(1)} = k_{y,P}^{(1)} = k_P^{(1)} \sin(\theta_v)\sin(\theta_h). \tag{14}$$

The wavenumbers $k_{z,P}^{(1)}$ and $k_{z,S}^{(1)}$ in the z direction for compressional and shear waves in the soil medium are given as

$$k_{z,P}^{(1)} = \sqrt{\left(k_P^{(1)}\right)^2 - \left(k^{(1)}\right)^2}, \quad k_{z,S}^{(1)} = \sqrt{\left(k_S^{(1)}\right)^2 - \left(k^{(1)}\right)^2}, \tag{15}$$

where $\mathrm{Re}\left(k_{z,\mathrm{P}}^{(1)}\right) > 0$ and $\mathrm{Re}\left(k_{z,\mathrm{S}}^{(1)}\right) > 0$ are taken for propagating waves (assuming $\omega > 0$). Furthermore, the total wavenumber $k^{(1)}$ in the horizontal plane (x, y) is defined as

$$k^{(1)} = \sqrt{\left(k_x^{(1)}\right)^2 + \left(k_y^{(1)}\right)^2}. \tag{16}$$

According to Snell's law for elastic waves [2], the wavenumbers in the x direction of the reflected compressional and shear waves are the same (equal to that of the incident wave), that is, $k_{x,\mathrm{P}}^{(1)} = k_{x,\mathrm{S}}^{(1)} = k_x^{(1)}$, as well as the wavenumbers in the y direction, that is, $k_{y,\mathrm{P}}^{(1)} = k_{y,\mathrm{S}}^{(1)} = k_y^{(1)}$.

Case 2: Incident shear wave type ψ. The plane-wave solutions for the incident ($\psi_{\mathrm{inc}}^{(1)}$) and reflected waves ($\phi_{\mathrm{ref}}^{(1)}$, $\psi_{\mathrm{ref}}^{(1)}$, $\chi_{\mathrm{ref}}^{(1)}$) are given as

$$\begin{aligned}
\psi_{\mathrm{inc}}^{(1)} &= \psi_0 \exp\left(-\mathrm{i}\,k_x^{(1)}x - \mathrm{i}\,k_y^{(1)}y - \mathrm{i}\,k_{z,\mathrm{S}}^{(1)}z\right), \\
\phi_{\mathrm{ref}}^{(1)} &= R_{\phi,\psi}\psi_0 \exp\left(-\mathrm{i}\,k_x^{(1)}x - \mathrm{i}\,k_y^{(1)}y + \mathrm{i}\,k_{z,\mathrm{P}}^{(1)}z\right), \\
\psi_{\mathrm{ref}}^{(1)} &= R_{\psi,\psi}\psi_0 \exp\left(-\mathrm{i}\,k_x^{(1)}x - \mathrm{i}\,k_y^{(1)}y + \mathrm{i}\,k_{z,\mathrm{S}}^{(1)}z\right), \\
\chi_{\mathrm{ref}}^{(1)} &= R_{\chi,\psi}\psi_0 \exp\left(-\mathrm{i}\,k_x^{(1)}x - \mathrm{i}\,k_y^{(1)}y + \mathrm{i}\,k_{z,\mathrm{S}}^{(1)}z\right),
\end{aligned} \tag{17}$$

where ψ_0 is the amplitude of the incident shear wave; $R_{\phi,\psi}$, $R_{\psi,\psi}$ and $R_{\chi,\psi}$ (given in Appendix A) are amplitude ratios of the reflected waves $\phi_{\mathrm{ref}}^{(1)}$, $\psi_{\mathrm{ref}}^{(1)}$ and $\chi_{\mathrm{ref}}^{(1)}$, to the incident shear wave $\psi_{\mathrm{inc}}^{(1)}$, respectively. The wavenumbers in the x and y directions in this case are given as

$$k_x^{(1)} = k_{x,\mathrm{S}}^{(1)} = -k_\mathrm{S}^{(1)} \sin\left(\theta_\mathrm{v}\right)\cos\left(\theta_\mathrm{h}\right), \; k_y^{(1)} = k_{y,\mathrm{S}}^{(1)} = k_\mathrm{S}^{(1)} \sin\left(\theta_\mathrm{v}\right)\sin\left(\theta_\mathrm{h}\right). \tag{18}$$

Here, it is noted that under the incident shear waves ($\psi_{\mathrm{inc}}^{(1)}$ and $\chi_{\mathrm{inc}}^{(1)}$) there exists a critical vertical incident angle, beyond which the wavenumber $k_{z,\mathrm{P}}^{(1)}$ becomes imaginary (see Eqs. (15) and (18)). This occurs when $k_\mathrm{P}^{(1)} < k^{(1)} = k_\mathrm{S}^{(1)}\sin(\theta_\mathrm{v})$. Therefore, the critical vertical angle is defined as

$$\theta_\mathrm{v}^{\mathrm{crit}} = \arcsin\left(\frac{k_\mathrm{P}^{(1)}}{k_\mathrm{S}^{(1)}}\right) = \arcsin\left(\sqrt{\frac{1-2\nu^{(1)}}{2-2\nu^{(1)}}}\right). \tag{19}$$

Evanescent waves are generated when $\theta_\mathrm{v} > \theta_\mathrm{v}^{\mathrm{crit}}$, and for those waves it is required that $\mathrm{Im}\left(k_{z,\mathrm{P}}^{(1)}\right) < 0$.

Case 3: Incident shear wave type χ. The plane-wave solutions for the incident ($\chi_{\mathrm{inc}}^{(1)}$) and reflected waves ($\phi_{\mathrm{ref}}^{(1)}$, $\psi_{\mathrm{ref}}^{(1)}$, $\chi_{\mathrm{ref}}^{(1)}$) are given as

$$\begin{aligned}
\chi_{\mathrm{inc}}^{(1)} &= \chi_0 \exp\left(-\mathrm{i}\,k_x^{(1)}x - \mathrm{i}\,k_y^{(1)}y - \mathrm{i}\,k_{z,\mathrm{S}}^{(1)}z\right), \\
\phi_{\mathrm{ref}}^{(1)} &= R_{\phi,\chi}\chi_0 \exp\left(-\mathrm{i}\,k_x^{(1)}x - \mathrm{i}\,k_y^{(1)}y + \mathrm{i}\,k_{z,\mathrm{P}}^{(1)}z\right), \\
\psi_{\mathrm{ref}}^{(1)} &= R_{\psi,\chi}\chi_0 \exp\left(-\mathrm{i}\,k_x^{(1)}x - \mathrm{i}\,k_y^{(1)}y + \mathrm{i}\,k_{z,\mathrm{S}}^{(1)}z\right), \\
\chi_{\mathrm{ref}}^{(1)} &= R_{\chi,\chi}\chi_0 \exp\left(-\mathrm{i}\,k_x^{(1)}x - \mathrm{i}\,k_y^{(1)}y + \mathrm{i}\,k_{z,\mathrm{S}}^{(1)}z\right),
\end{aligned} \tag{20}$$

where χ_0 is the amplitude of the incident shear wave; $R_{\phi,\chi}$, $R_{\psi,\chi}$ and $R_{\chi,\chi}$ (given in Appendix A) are amplitude ratios of the reflected waves $\phi_{\mathrm{ref}}^{(1)}$, $\psi_{\mathrm{ref}}^{(1)}$ and $\chi_{\mathrm{ref}}^{(1)}$, to the incident shear wave $\chi_{\mathrm{inc}}^{(1)}$, respectively. The wavenumbers in the x and y directions in this case are the same as that in case 2; see Eq. (18).

3.2. Scattering of elastic waves by the tunnel

The presence of the infinitely long cylindrical tunnel causes scattering of elastic waves. These scattered waves are denoted as $\phi_{\mathrm{s},1}^{(1)}$, $\psi_{\mathrm{s},1}^{(1)}$ and $\chi_{\mathrm{s},1}^{(1)}$. The subscript "s, 1" indicates the 'directly scattered' waves propagating away from the tunnel in the half-space. When these directly scattered waves meet the free surface of the half-space, secondary scattered waves are generated, which are denoted as $\phi_{\mathrm{s},2}^{(1)}$, $\psi_{\mathrm{s},2}^{(1)}$ and $\chi_{\mathrm{s},2}^{(1)}$. The subscript "s, 2" indicates the 'secondary scattered' waves. Based on the spirit of the method of images, these secondary scattered waves

are considered to originate from an image source, but the intensity is a priori unknown. The image source is located at the centre of the image of the tunnel, positioned symmetrically with respect to the free surface.

To describe the waves propagating away from the tunnel and its image, we apply the method of separation of variables to solve the Helmholtz equations shown in Eq. (8), assuming a harmonic variation in the circumferential direction of the form $\exp(\mathrm{i}\,n\theta)$ [4,33]. To satisfy the continuity condition at $\theta = 0$ and $\theta = 2\pi$, n is required to be an integer. It turns out that, for fixed n, the radial behaviour is described by a Hankel function. The general solution is then constructed as an infinite series (that is commonly referred to as a wave-function expansion), which represents the entire scattered wave field. The potentials related to the scattered wave fields in the half-space are given as follows:

$$\begin{aligned}
\phi_{\mathrm{s},1}^{(1)} &= \sum_{n=-\infty}^{\infty} a_n H_n^{(2)}\left(k_\mathrm{a}^{(1)}r_1\right)\exp\left(\mathrm{i}\,n\theta_1 - \mathrm{i}\,k_x^{(1)}x\right), \\
\psi_{\mathrm{s},1}^{(1)} &= \sum_{n=-\infty}^{\infty} b_n H_n^{(2)}\left(k_\mathrm{b}^{(1)}r_1\right)\exp\left(\mathrm{i}\,n\theta_1 - \mathrm{i}\,k_x^{(1)}x\right), \\
\chi_{\mathrm{s},1}^{(1)} &= \sum_{n=-\infty}^{\infty} c_n H_n^{(2)}\left(k_\mathrm{b}^{(1)}r_1\right)\exp\left(\mathrm{i}\,n\theta_1 - \mathrm{i}\,k_x^{(1)}x\right), \\
\phi_{\mathrm{s},2}^{(1)} &= \sum_{n=-\infty}^{\infty} d_n H_n^{(2)}\left(k_\mathrm{a}^{(1)}r_2\right)\exp\left(\mathrm{i}\,n\theta_2 - \mathrm{i}\,k_x^{(1)}x\right), \\
\psi_{\mathrm{s},2}^{(1)} &= \sum_{n=-\infty}^{\infty} e_n H_n^{(2)}\left(k_\mathrm{b}^{(1)}r_2\right)\exp\left(\mathrm{i}\,n\theta_2 - \mathrm{i}\,k_x^{(1)}x\right), \\
\chi_{\mathrm{s},2}^{(1)} &= \sum_{n=-\infty}^{\infty} f_n H_n^{(2)}\left(k_\mathrm{b}^{(1)}r_2\right)\exp\left(\mathrm{i}\,n\theta_2 - \mathrm{i}\,k_x^{(1)}x\right),
\end{aligned} \tag{21}$$

where $a_n, \ldots, f_n$ denote the unknown coefficients which will be determined from the boundary and interface conditions, and $H_n^{(2)}(..)$ denotes the Hankel function of the second kind and n-th order, and represents outgoing waves (propagating away from the tunnel) considering the time dependent factor $\mathrm{e}^{+\mathrm{i}\,\omega t}$. $k_\mathrm{a}^{(1)}$ and $k_\mathrm{b}^{(1)}$ are the cylindrical wavenumbers of the compressional and shear waves in the soil, respectively:

$$k_\mathrm{a}^{(1)} = \sqrt{\left(k_\mathrm{P}^{(1)}\right)^2 - \left(k_x^{(1)}\right)^2}, \; k_\mathrm{b}^{(1)} = \sqrt{\left(k_\mathrm{S}^{(1)}\right)^2 - \left(k_x^{(1)}\right)^2}, \tag{22}$$

where $\mathrm{Re}(k_\mathrm{a}^{(1)}) > 0$ and $\mathrm{Re}(k_\mathrm{b}^{(1)}) > 0$ are taken for the propagating cylindrical waves in the soil (assuming $\omega > 0$), while $\mathrm{Im}(k_\mathrm{a}^{(1)}) < 0$ is taken for the evanescent cylindrical waves. Note that cylindrical S waves in the soil never become evanescent because $k_\mathrm{b}^{(1)}$ is real valued as $k_\mathrm{S}^{(1)}$ is always larger than $k_x^{(1)}$.

The potentials related to refracted waves in the tunnel are constructed using Bessel functions, and are given as

$$\begin{aligned}
\phi_{\mathrm{r}}^{(2)} &= \sum_{n=-\infty}^{\infty} \left[g_n J_n\left(k_\mathrm{a}^{(2)}r_1\right) + h_n Y_n\left(k_\mathrm{a}^{(2)}r_1\right)\right]\exp\left(\mathrm{i}\,n\theta_1 - \mathrm{i}\,k_x^{(2)}x\right), \\
\psi_{\mathrm{r}}^{(2)} &= \sum_{n=-\infty}^{\infty} \left[i_n J_n\left(k_\mathrm{b}^{(2)}r_1\right) + j_n Y_n\left(k_\mathrm{b}^{(2)}r_1\right)\right]\exp\left(\mathrm{i}\,n\theta_1 - \mathrm{i}\,k_x^{(2)}x\right), \\
\chi_{\mathrm{r}}^{(2)} &= \sum_{n=-\infty}^{\infty} \left[k_n J_n\left(k_\mathrm{b}^{(2)}r_1\right) + l_n Y_n\left(k_\mathrm{b}^{(2)}r_1\right)\right]\exp\left(\mathrm{i}\,n\theta_1 - \mathrm{i}\,k_x^{(2)}x\right),
\end{aligned} \tag{23}$$

where $g_n, \ldots, l_n$ denote the unknown coefficients; $J_n(..)$ and $Y_n(..)$ denote the Bessel functions of the first and second kind, respectively, and n-th order. $k_\mathrm{a}^{(2)}$ and $k_\mathrm{b}^{(2)}$ are the wavenumbers of the compressional and shear cylindrical waves in the tunnel, respectively:

$$k_\mathrm{a}^{(2)} = \sqrt{\left(k_\mathrm{P}^{(2)}\right)^2 - \left(k_x^{(2)}\right)^2}, \; k_\mathrm{b}^{(2)} = \sqrt{\left(k_\mathrm{S}^{(2)}\right)^2 - \left(k_x^{(2)}\right)^2}, \tag{24}$$

The longitudinal wavenumber $k_x^{(2)}$ of the refracted waves is equal to $k_x^{(1)}$ according to Snell's law. Note that here we use Bessel functions to represent the cylindrical waves in the tunnel. Alternatively, we could use the Hankel functions of the first and second kind ($H_n^{(1)}$ and $H_n^{(2)}$) to represent the cylindrical ingoing and outgoing waves in the tunnel, like in [32]. Mathematically, both representations of the waves in the tunnel are correct. However, it is found that the numerical results obtained by using Bessel functions are more accurate; see Sections 7.2 and 8.2.

3.3. Total wave fields

The incident and reflected plane waves together with the directly and secondary scattered cylindrical waves make up the total wave field in the half-space ($\phi^{(1)}$, $\psi^{(1)}$ and $\chi^{(1)}$):

$$
\begin{aligned}
\phi^{(1)} &= \phi_{\text{inc}}^{(1)} + \phi_{\text{ref}}^{(1)} + \phi_{\text{s},1}^{(1)} + \phi_{\text{s},2}^{(1)}, \\
\psi^{(1)} &= \psi_{\text{inc}}^{(1)} + \psi_{\text{ref}}^{(1)} + \psi_{\text{s},1}^{(1)} + \psi_{\text{s},2}^{(1)}, \\
\chi^{(1)} &= \chi_{\text{inc}}^{(1)} + \chi_{\text{ref}}^{(1)} + \chi_{\text{s},1}^{(1)} + \chi_{\text{s},2}^{(1)}.
\end{aligned}
\tag{25}
$$

The total wave field in the tunnel consists of the refracted waves ($\phi^{(2)}$, $\psi^{(2)}$ and $\chi^{(2)}$):

$$
\phi^{(2)} = \phi_{\text{r}}^{(2)}, \quad \psi^{(2)} = \psi_{\text{r}}^{(2)}, \quad \chi^{(2)} = \chi_{\text{r}}^{(2)}.
\tag{26}
$$

4. Stress and displacement expressions in terms of complex variables

To employ the complex-variable theory for determining the unknown coefficients in Eqs. (21) and (23), we introduce a complex variable $\kappa = y + \mathrm{i}\, z = r e^{\mathrm{i}\theta}$ and its conjugate $\bar{\kappa} = y - \mathrm{i}\, z = r e^{-\mathrm{i}\theta}$, where y, z and r, θ are the dimensionless Cartesian and cylindrical coordinates in the vertical plane, respectively, as introduced in Section 2. In line with the introduction of the image source, the local coordinate systems (y_1, z_1, x_1) and (y_2, z_2, x_2) are defined symmetrically with respect to the free surface of the half-space, with z_2 positive downward (see Fig. 1). The local coordinates r_1 and r_2 can be written in terms of complex variables κ and $\bar{\kappa}$ related to the global coordinate system using the relation between different coordinates:

$$
\begin{aligned}
r_1 &= |y_1 + \mathrm{i}\, z_1| = |y + \mathrm{i}(z + H)| = |\kappa + \mathrm{i}\, H|, \\
r_2 &= |y_2 + \mathrm{i}\, z_2| = |y + \mathrm{i}(-z + H)| = |\bar{\kappa} + \mathrm{i}\, H|.
\end{aligned}
\tag{27}
$$

The exponential terms of the local coordinates θ_1 and θ_2, showing up in Eqs. (21) and (23), can also be written in terms of the complex variables κ and $\bar{\kappa}$ as

$$
e^{\mathrm{i}\theta_1} = \frac{y_1 + \mathrm{i}\, z_1}{r_1} = \frac{\kappa + \mathrm{i}\, H}{|\kappa + \mathrm{i}\, H|}, \quad e^{\mathrm{i}\theta_2} = \frac{y_2 + \mathrm{i}\, z_2}{r_2} = \frac{\bar{\kappa} + \mathrm{i}\, H}{|\bar{\kappa} + \mathrm{i}\, H|}.
\tag{28}
$$

Substituting Eqs. (27) and (28) into the expressions for the potentials (see Eqs. (21) and (23)), we get the potentials in terms of the complex variables κ and $\bar{\kappa}$, which are not shown in this paper for brevity.

Thereafter, the displacement (see Eq. (10)) and stress components in the Cartesian coordinates (y, z, x) can also be expressed in terms of the complex variables κ and $\bar{\kappa}$, and they are shown in Eqs. (B.1)–(B.9) in Appendix B. The expressions for the displacements and stresses in the cylindrical coordinate system (r, θ, x) can be derived in terms of the complex variables κ and $\bar{\kappa}$ as well by employing the transformation relations (see Eqs. (11)–(12)), and they are shown in Eqs. (B.10)–(B.16).

5. Conformal mapping

As shown in Fig. 1, there are two different types of boundary surfaces in the model (i.e., a flat free surface and cylindrical surfaces of the tunnel). This makes the boundary value problem difficult to solve. In this paper, we propose to use conformal mapping functions to circumvent this difficulty by mapping the original domain with boundary surfaces of two different types onto an image domain with boundary surfaces of the same type. The application of conformal mapping functions is demonstrated in this section.

We have introduced the complex variable κ and its conjugate $\bar{\kappa}$ in the original physical domain in Section 4. Here, we introduce a complex variable $\zeta = \xi + \mathrm{i}\eta = \rho e^{\mathrm{i}\vartheta}$ and its conjugate $\bar{\zeta} = \xi - \mathrm{i}\eta = \rho e^{-\mathrm{i}\vartheta}$, which are defined in the image domain. Two conformal mapping functions $w^{(1)}(\zeta)$ and $w^{(2)}(\zeta)$, one for the region of the half-space with a cavity and one for the tunnel region, defining the relations between the two
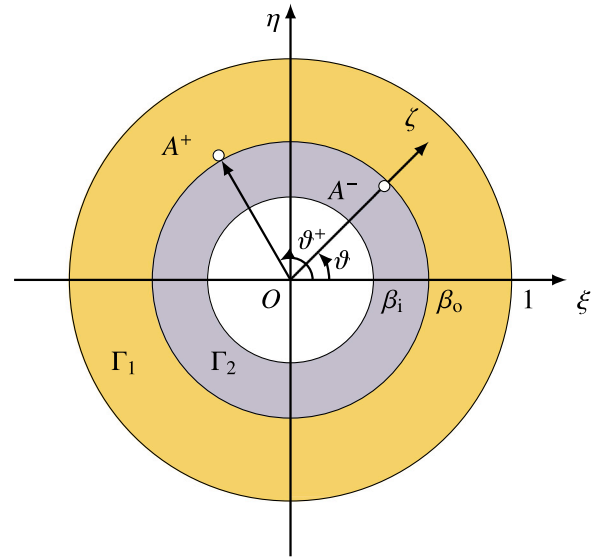

Fig. 3. Image domain.

complex variables κ and ζ in the original and image domains, are given as follows:

$$
\kappa^{(1)} = w^{(1)}(\zeta) = -\mathrm{i}\, G \frac{1 + \zeta}{1 - \zeta},
\tag{29}
$$

$$
\kappa^{(2)} = w^{(2)}(\zeta) = -\mathrm{i}\, H + \frac{R_{\text{o}}}{\beta_{\text{o}}} \zeta,
\tag{30}
$$

where $G = H\left(1 - \beta_{\text{o}}^2\right) \big/ \left(1 + \beta_{\text{o}}^2\right)$ and $\beta_{\text{o}} = H/R_{\text{o}} - \sqrt{\left(H/R_{\text{o}}\right)^2 - 1}$. Using these two mapping functions, the two regions Ω_1 and Ω_2 in the physical domain (as shown in Fig. 1) are mapped onto two regions Γ_1 and Γ_2 in the image domain (as shown in Fig. 3), respectively. Accordingly, the free surface of the half-space $z = 0$, the outer surface $r_1 = R_{\text{o}}$ and inner surface $r_1 = R_{\text{i}}$ of the tunnel correspond to surfaces defined by circles $|\zeta| = 1$, $|\zeta| = \beta_{\text{o}}$ and $|\zeta| = \beta_{\text{i}} = \beta_{\text{o}} R_{\text{i}}/R_{\text{o}}$. Clearly, the boundary surfaces in the image domain are of the same type.

The mappings of the regions Ω_1 and Ω_2 in the physical domain onto regions Γ_1 and Γ_2 in the image domain are conformal and reversible. It can be easily proven that the mapping functions $w^{(1)}(\zeta)$ and $w^{(2)}(\zeta)$ are analytic (except at one point ($\rho = 1$, $\vartheta = 0$) corresponding to points at infinity in the physical domain), and their derivatives with respect to the complex variable ζ (i.e., $w^{(1)'}(\zeta)$ and $w^{(2)'}(\zeta)$) are nonzero.

In general, the mapping functions induce a phase change between the complex variables in the two domains. For a general conformal mapping function $\kappa = w(\zeta)$, the relation between the coordinate θ in the physical domain and the coordinate ϑ in the image domain is defined as [28]

$$
\exp(\mathrm{i}\,\theta) = \frac{\zeta}{\rho} \frac{w'(\zeta)}{|w'(\zeta)|} = \exp(\mathrm{i}\,\vartheta) \frac{w'(\zeta)}{|w'(\zeta)|}.
\tag{31}
$$

The first conformal mapping function $w^{(1)}(\zeta)$ indeed induces a phase change because $w^{(1)'}(\zeta)$ is a complex number. On the contrary, the second mapping function $w^{(2)}(\zeta)$ does not induce a phase change because the $w^{(2)'}(\zeta)$ is a constant (i.e., $\frac{w'(\zeta)}{|w'(\zeta)|} = 1$, $\exp(\mathrm{i}\,\theta) = \exp(\mathrm{i}\,\vartheta)$; see Eq. (31)).

As a consequence, point A at the tunnel–soil interface (see Fig. 1) is mapped onto two different points A^+ and A^- (as shown in Fig. 3) using mapping functions $w^{(1)}(\zeta)$ and $w^{(2)}(\zeta)$, respectively. When we apply the continuity conditions at the tunnel–soil interface (see Section 6), we need to take this issue into account. Let ϑ^+ and ϑ denote the arguments of the vectors $\overrightarrow{OA^+}$ and $\overrightarrow{OA^-}$ in the image domain, respectively. The relation between these two angles can be derived using $\kappa^{(1)} = \kappa^{(2)}$:

$$
-\mathrm{i}\, G \frac{1 + \beta_{\text{o}} e^{\mathrm{i}\vartheta^+}}{1 - \beta_{\text{o}} e^{\mathrm{i}\vartheta^+}} = -\mathrm{i}\, H + \frac{R_{\text{o}}}{\beta_{\text{o}}} \beta_{\text{o}} e^{\mathrm{i}\vartheta},
\tag{32}
$$

and is given as

$$\vartheta^+(\vartheta) = \arg\left[\frac{i R_o e^{i\vartheta} + H - G}{i R_o e^{i\vartheta} + H + G}\right]. \tag{33}$$

6. Solving the unknown coefficients

As shown in Section 4, the potentials, displacements and stresses are written in terms of complex variables κ and $\bar{\kappa}$. The derivatives of potentials related to the plane waves with respect to κ and $\bar{\kappa}$ can be obtained by simply applying the chain rule (i.e., first with respect to y and z, and then to κ and $\bar{\kappa}$), and the derivatives of potentials related to cylindrical waves with respect to the complex variables can be derived using both the chain rule and the recurrence relations of Hankel/Bessel functions (see Appendix C).

To solve the problem in the image domain where the boundary surfaces are of the same type, we need to get the expressions for displacements and stresses in terms of the complex variables ζ and $\bar{\zeta}$. Applying the derivatives of potentials with respect to κ and $\bar{\kappa}$ and then replacing the complex variables κ and $\bar{\kappa}$ by the appropriate mapping function (see Eqs. (29) and (30)) and their conjugates, we can get the potentials, displacements and stresses written in terms of ζ and $\bar{\zeta}$; they are not shown in this paper for brevity.

Considering the total wave field in the half-space and tunnel (see Eqs. (25) and (26)), and using the expressions for displacements and stresses in terms of complex variables ζ and $\bar{\zeta}$, we obtain a set of algebraic equations based on the boundary and continuity conditions (see Eq. (9)):

$$\sum_{i=1}^{12}\sum_{n=-\infty}^{\infty} k_n^{(j,i)}(\vartheta)x_n^{(i)} = b^{(j)}(\vartheta), \tag{34}$$

where $x_n^{(1)} = a_n, \ldots, x_n^{(12)} = l_n$; $i = \{1, \ldots, 12\}$ indicates the term related to the corresponding potentials of cylindrical waves; see Eqs. (21) and (23). $j = \{1, \ldots, 12\}$ denotes the specific boundary condition: $j = \{1, 2, 3\}$ and $j = \{4, 5, 6\}$ refer to the stress-free boundary conditions at the half-space surface and at the inner surface of the tunnel, respectively; $j = \{7, \ldots, 12\}$ refer to the continuity conditions at the tunnel–soil interface; see Eq. (9). Not all the entries of $k_n^{(j,i)}$ and $b^{(j)}$ are presented in this paper, but they are understood as functions of complex variables ζ and $\bar{\zeta}$. For the aim of demonstration, we present the entries of $k_n^{(j,i)}$ and $b^{(j)}$ related to the tenth continuity condition (i.e., $\sigma_{r_1\theta_1}^{(1)} = \sigma_{r_1\theta_1}^{(2)}$) in Appendix D. In addition, for the set of algebraic equations ($j = \{7, \ldots, 12\}$) formulated based on the continuity conditions, all the displacements and stresses related to the soil medium, namely, $u_{r_1}^{(1)}, u_{\theta_1}^{(1)}, u_{x_1}^{(1)}, \sigma_{r_1 r_1}^{(1)}, \sigma_{r_1\theta_1}^{(1)}$ and $\sigma_{r_1 x_1}^{(1)}$, are functions of $\vartheta^+(\vartheta)$ while those related to the tunnel are functions of ϑ (see also Section 5).

Multiplying Eq. (34) by the complex conjugate of the circumferential basis functions $\exp(i n\vartheta)$, which appears in the expression for the potentials of the cylindrical waves, integrating over the interval $[0, 2\pi]$ and applying the orthogonality relation wherever possible, we get

$$\sum_{i=1}^{12}\sum_{n=-\infty}^{\infty} k_{n,s}^{(j,i)} x_n^{(i)} = b_s^{(j)}, \tag{35}$$

where $s = \{0, \pm1, \pm2, \ldots\}$ and

$$k_{n,s}^{(j,i)} = \frac{1}{2\pi}\int_0^{2\pi} k_n^{(j,i)}(\vartheta)\exp(-i s\vartheta)\,d\vartheta, \tag{36}$$

$$b_s^{(j)} = \frac{1}{2\pi}\int_0^{2\pi} b^{(j)}(\vartheta)\exp(-i s\vartheta)\,d\vartheta. \tag{37}$$

For the potentials related to the directly scattered waves in the half-space ($\phi_{s,1}^{(1)}, \psi_{s,1}^{(1)}, \chi_{s,1}^{(1)}$ in Eq. (21)) and for the potentials related to the refracted waves in the tunnel (Eq. (23)), orthogonality of the exponential functions can be employed (i.e., $k_{n,s}^{(j,i)} = 0$ for $s \neq n$, and $i = \{1, 2, 3, 7, \ldots, 12\}$). The maximum values of n and s need to be finite in order to be able to evaluate the unknown coefficients, which means

that the sum over circumferential modes needs to be truncated. The amount of modes for refracted waves in the tunnel is $2N + 1$ when we consider n from $-N$ to N. If we use the same amount of modes $2N + 1$ for both the directly scattered waves ($\phi_{s,1}^{(1)}, \psi_{s,1}^{(1)}, \chi_{s,1}^{(1)}$) and secondary scattered waves ($\phi_{s,2}^{(1)}, \psi_{s,2}^{(1)}, \chi_{s,2}^{(1)}$), we use the following multiplication function:

$$\exp(-i s\vartheta), \ j = \{1, \ldots, 12\}; \ s = \{0, \pm1, \pm2, \ldots, \pm N\}. \tag{38}$$

The matrix equation that is formulated based on Eq. (35) becomes

$$[\mathbf{K}]_{12(2N+1)\times 12(2N+1)} [\mathbf{x}]_{12(2N+1)\times 1} = [\mathbf{b}]_{12(2N+1)\times 1}. \tag{39}$$

If we use $2N + 1$ modes for the directly scattered waves and $2M + 1$ ($M \neq N$) modes for the secondary scattered waves, in order to still formulate a square matrix, different rows in Eq. (34) are multiplied by different multiplication functions, respectively, as follows:

$$\exp(-i s_D\vartheta), \ j = \{1, \ldots, 3\}; s_D = \{0, \pm1, \pm2, \ldots, \pm M\},$$
$$\exp(-i s\vartheta), \quad j = \{4, \ldots, 12\}; s = \{0, \pm1, \pm2, \ldots, \pm N\}, \tag{40}$$

and the matrix equation obtained from Eq. (35) reads

$$[\mathbf{K}]_{(9(2N+1)+3(2M+1))\times(9(2N+1)+3(2M+1))} [\mathbf{x}]_{(9(2N+1)+3(2M+1))\times 1}$$
$$= [\mathbf{b}]_{(9(2N+1)+3(2M+1))\times 1}. \tag{41}$$

By using different numbers of modes for the directly and secondary scattered waves, we acknowledge their contributions to the final response in the system. It can be shown that, for converged results at the tunnel, more circumferential modes of the directly scattered waves are needed than of the secondary scattered waves (i.e., $N > M$), while for converged results at the ground surface, more circumferential modes of the secondary scattered waves are needed. This is because, due to geometrical attenuation, the potentials have larger contributions to the response in the near field than in the far field. An advantage of using a different number of circumferential modes is that the size and condition of the matrix $\mathbf{K}$ can be smaller, and the computation time can be reduced.

Matlab is used to solve for the unknown coefficients. The calculation is performed on a laptop with CPU of Intel Core i7 5600U/2.6 GHz. For example, the computation time varies from 15 s to 2 min depending on the value of N (and M, if different) from 3 to 10, respectively, for a tunnel embedded in a half-space (3D case) using the first set of parameters in Table 1. Since the computation is very efficient even when using large values of N and M, the same number of circumferential modes for both wave fields will be used in the following analysis (i.e., we use the multiplication function in Eq. (38) instead of the one in Eq. (40)).

From the analysis using the proposed method, we find that matrix $\mathbf{K}$ may have a relatively high condition number. That happens particularly when Hankel functions have small arguments (i.e., when one of the cylindrical wavenumbers $k_a^{(1)}, k_b^{(1)}, k_a^{(2)}$ and $k_b^{(2)}$ is relatively small, see Eqs. (21) and (23)), see explanation in Section 7.2.

7. Convergence tests and validations

This section presents convergence tests and validations of the present method by comparing with results obtained by other methods. Three categories of comparisons are discussed: 2D anti-plane shear (SH waves), 2D plane-strain (P and SV waves) and 3D cases. Table 1 presents the five parameter sets comprising parameters of the soil and tunnel, the geometries of the system and the frequencies of the incident harmonic waves.

In Table 1, $\tilde{E}^{(1)}$ and $\tilde{E}^{(2)}$ are the Young's moduli of the soil and tunnel, respectively, $\nu^{(1,2)}$ are the Poisson's ratios, and h is the thickness of the tunnel. $\eta = \tilde{\omega}\tilde{R}_o\left/\left(\pi\tilde{c}_S^{(1)}\right)\right.$ is the dimensionless frequency used in the literature [10], which is different from the dimensionless frequency ω introduced in this paper (see Eq. (7)).
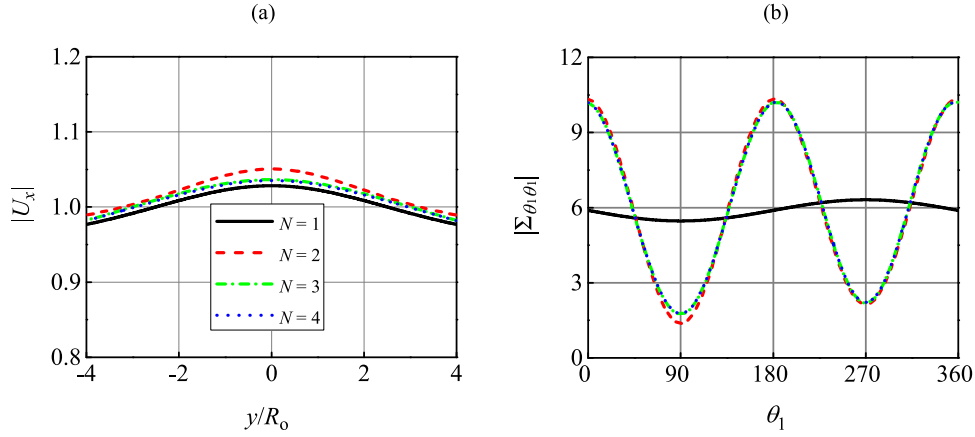
Fig. 4. Convergence tests: (a) longitudinal displacement U_x at the half-space surface $z = 0$ and (b) hoop stress $\Sigma_{\theta_1\theta_1}$ at $r_1 = R_o$. The first parameter set in Table 1 is used for a 3D problem with an incident P wave, $\theta_v = 30°$ and $\theta_h = 0°$.

Table 1
Five sets of parameters of the system.

Parameter sets	Soil parameters	Tunnel parameters	Geometries and frequencies
① Liu et al. [13]	$\tilde{E}^{(1)} = 7.567$ GPa $\nu^{(1)} = 0.333$ $\tilde{\rho}^{(1)} = 2664$ kg/m³	$\tilde{E}^{(2)} = 16$ GPa $\nu^{(2)} = 0.2$ $\tilde{\rho}^{(2)} = 2240$ kg/m³	$H = 5R_i$ $h = 0.1R_i$ $\eta = 0.105$
② Lee et al. [34]	$\tilde{E}^{(1)} = 0.29593$ GPa $\nu^{(1)} = 0.333$ $\tilde{\rho}^{(1)} = 1640$ kg/m³	$\tilde{E}^{(2)} = 0.7992$ GPa $\nu^{(2)} = 0.2$ $\tilde{\rho}^{(2)} = 3 \times \tilde{\rho}^{(1)}$	$H = 1.5R_o$ $h = 0.1R_o$ $\eta = 0.5$
③ Balendra et al. [19]	$\tilde{\mu}^{(1)} = 0.111$ GPa $\tilde{c}_s^{(1)} = 260$ m/s $\tilde{\rho}^{(1)} = 1640$ kg/m³	$\tilde{\mu}^{(2)} = 8.4$ GPa $\nu^{(2)} = 0.2$ $\tilde{\rho}^{(2)} = 2410$ kg/m³	$H = 2.5R_o$ $h = 0.1R_o$ $\eta = 0.245$
④ Datta et al. [35]	$\tilde{E}^{(1)} = 0.69$ Gpa $\nu^{(1)} = 0.45$ $\tilde{\rho}^{(1)} = 2665$ kg/m³	$\tilde{E}^{(2)} = 16$ GPa $\nu^{(2)} = 0.2$ $\tilde{\rho}^{(2)} = 2240$ kg/m³	$H = 8.33R_i$ $h = 0.1R_i$ $\eta = 0.132$
⑤ Wong et al. [24,25]	$\tilde{E}^{(1)} = 0.69$ GPa $\nu^{(1)} = 0.45$ $\tilde{\rho}^{(1)} = 2665$ kg/m³	$\tilde{E}^{(2)} = 16$ GPa $\nu^{(2)} = 0.2$ $\tilde{\rho}^{(2)} = 2240$ kg/m³	$H = 2R_i$ $h = 0.1R_i$ $\eta = 0.132$

For results presented in the following, all displacements and stresses are normalised. The displacement components are normalised by the amplitude of the incident compressional (P) or shear (S) wave:

$$U = u/U_{\{P,S\}}, \tag{42}$$

where u denotes an arbitrary (but corresponding to U) displacement component, and U_P and U_S are the amplitudes of the corresponding incident P and S waves, respectively, which can be derived using Eq. (10):

$$\begin{aligned} U_P &= i\,k_P^{(1)}\phi_0, \\ U_S &= i\,k_b^{(1)}\psi_0 \text{ or } U_S = k_b^{(1)}\chi_0. \end{aligned} \tag{43}$$

The normalised stress is given as

$$\Sigma = \sigma \Big/ \Big[\omega\rho^{(1)}c_S^{(1)}U_{\{P,S\}}\Big], \tag{44}$$

where σ denotes an arbitrary (but corresponding to Σ) stress component.

For a 3D problem, a convergence test using the first parameter set in Table 1 is shown in Fig. 4. The system is subject to an incident P wave ($\eta = 0.105$, $\tilde{f} = 10.84$ Hz). The vertical and horizontal incident angles are $\theta_v = 30°$ and $\theta_h = 0°$. It is shown that both the normalised displacement U_x at the half-space surface $z = 0$ and the normalised hoop stress $\Sigma_{\theta_1\theta_1}$ at $r_1 = R_o$ converge very quickly. It can be verified that for relatively high frequencies, $N = 5$ appears sufficient. All the

results in this paper are obtained using $N = 5$ and employing the representations of cylindrical waves in the tunnel in terms of Bessel functions (see Eq. (23)) unless specified otherwise. The remainder of this section is devoted to validations.

7.1. 2D anti-plane shear cases

This subsection presents the following three comparisons. We consider a problem of a tunnel embedded in a half-space subjected to incident SH waves (i.e., $\chi_{inc}^{(1)}$) using the parameter sets in Table 1. In the following Figs. 5–11, the black solid line indicates the present results while the red dashed line indicates the results taken from the literature.

The first comparison is made with the results obtained by Lee and Trifunac [34] for a vertically incident SH wave ($\theta_v = 0°$ and $\theta_h = 90°$). The second parameter set in Table 1 is used. The longitudinal displacement U_x at the half-space surface $z = 0$, the longitudinal displacement U_{x1} and shear stress $\Sigma_{r_1x_1}$ at the tunnel–soil interface $r_1 = R_o$, and the shear stress $\Sigma_{\theta_1x_1}$ at the inner surface of the tunnel $r_1 = R_i$ are shown in Fig. 5. An excellent agreement between the present results and those from [34] is observed.

The responses in Fig. 5 are symmetric with respect to 90° and 270° as expected based on the excitation. In Fig. 5(a), we observe the screening effect of the tunnel, as the longitudinal displacement is smaller in the range of $y/R_o = [-2, 2]$ above the tunnel. Comparing Fig. 5(c) and (d), we observe that the magnitude of $\Sigma_{\theta_1x_1}$ is much larger than that of $\Sigma_{r_1x_1}$.

The second comparison is made between the present results and those obtained by Balendra et al. [19] for a non-vertically incident SH wave ($\theta_v = 30°$ and $\theta_h = 90°$). The same quantities as in the previous example are shown in Fig. 6, but the shear stress is normalised differently for consistency with the literature result: $\Sigma_{\theta_1x_1} = \left|2\sigma_{\theta_1x_1}/[(1-\nu^{(2)})\omega\rho^{(1)}c_S^{(1)}U_S]\right|$. A very good agreement is observed. For this obliquely incident SH wave ($\theta_v = 30°$), the response loses symmetry (compare Figs. 5 and 6). In Fig. 6(a), we observe that the response is smaller to the right of the tunnel due to the screening effect. Fig. 6(d) shows that the shear stress $\Sigma_{\theta_1x_1}$ is amplified much more than $\Sigma_{r_1x_1}$ (this is also the case when the original normalisation is used), which is the same as in the first example.

For the third comparison, we consider the first parameter set in Table 1 and validate the current results with the results obtained by Liu et al. [13], and by Barros and Luco [10]. The system is subjected to a vertically incident wave ($\theta_v = 0°$ and $\theta_h = 90°$). We observe an excellent agreement; see Fig. 7. The normalisation factor for $\Sigma_{\theta_1x_1}$ is taken the same as in the previous example. It is interesting to note that the screening effect is not observed in the third example, and the maximum displacement occurs above the tunnel. The reason is that the frequency is lower and the tunnel is embedded deeper in the third
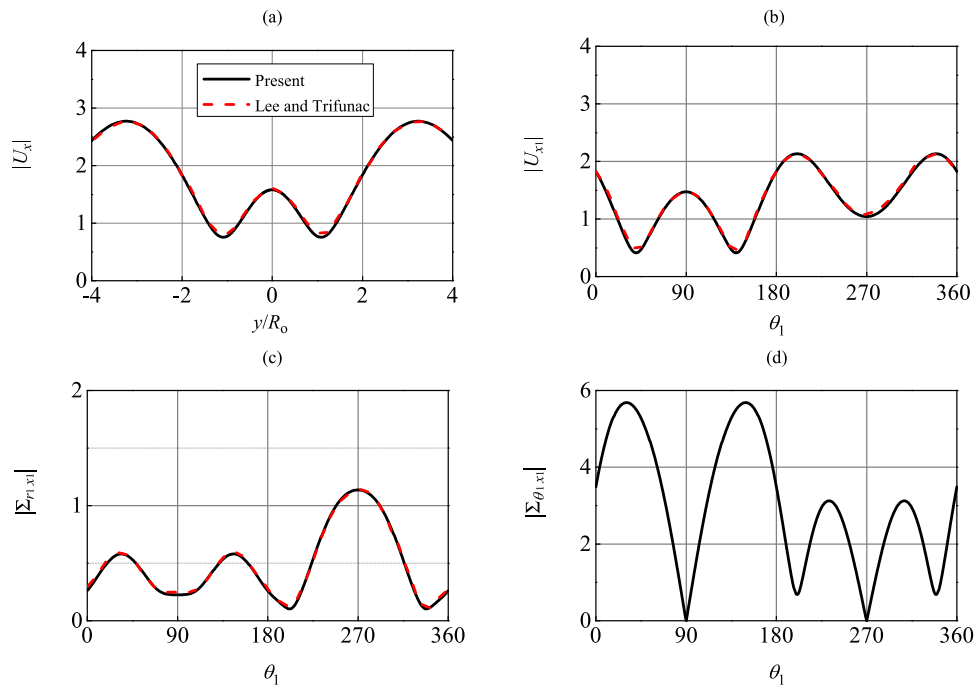
Fig. 5. The first comparison example for the 2D SH wave case ($\chi_{inc}^{(1)}$): (a) U_x at $z = 0$, (b) U_{x_1} at $r_1 = R_o$, (c) $\Sigma_{r_1 x_1}$ at $r_1 = R_o$ and (d) $\Sigma_{\theta_1 x_1}$ at $r_1 = R_i$. The excitation is a vertically incident SH wave ($\theta_v = 0°$ and $\theta_h = 90°$), and the second parameter set in Table 1 is used. Note that for panel (d) no result from literature is available.

Fig. 6. The second comparison example for the 2D SH wave case ($\chi_{inc}^{(1)}$): (a) U_x at $z = 0$, (b) U_{x_1} at $r_1 = R_o$, (c) $\Sigma_{r_1 x_1}$ at $r_1 = R_o$ and (d) $\Sigma_{\theta_1 x_1}$ at $r_1 = R_i$. The excitation is a non-vertically incident SH wave ($\theta_v = 30°$ and $\theta_h = 90°$), and the third parameter set in Table 1 is used. Note that for panel (a) no result from literature is available.

example ($\eta = 0.105$, $H = 5R_i = 4.545R_o$) than in the first example ($\eta = 0.5$, $H = 1.5R_o$). We can see that the screening effect is also not observed for another example, which uses the fourth parameter set ($\eta = 0.132$, $H = 8.33R_i$) in Table 1; see Fig. 8(c) and (f).

By comparing the first and third examples in this subsection, we see that the distributions and amplitudes of the responses are quite different in these two examples even though they are both subject to

vertically incident SH waves. That is because the system parameters (i.e., the dimensionless frequency, the stiffness ratio of the tunnel to soil, and the embedded depth of the tunnel) are different. We will discuss the effect of these and other two parameters (the vertical incident angle and the thickness of the tunnel) on the response of the system in Section 8.
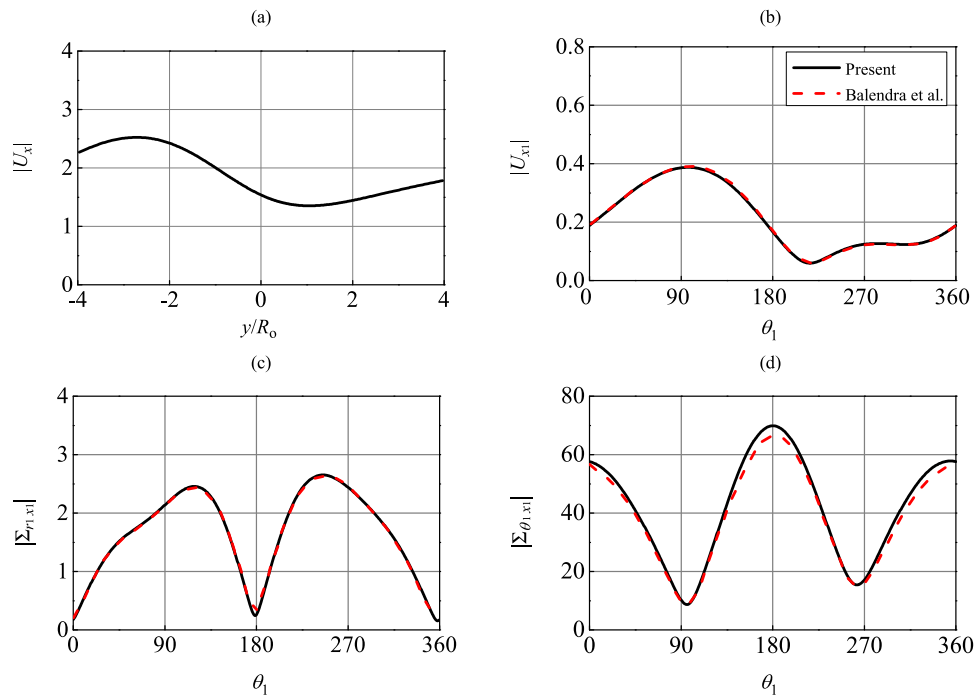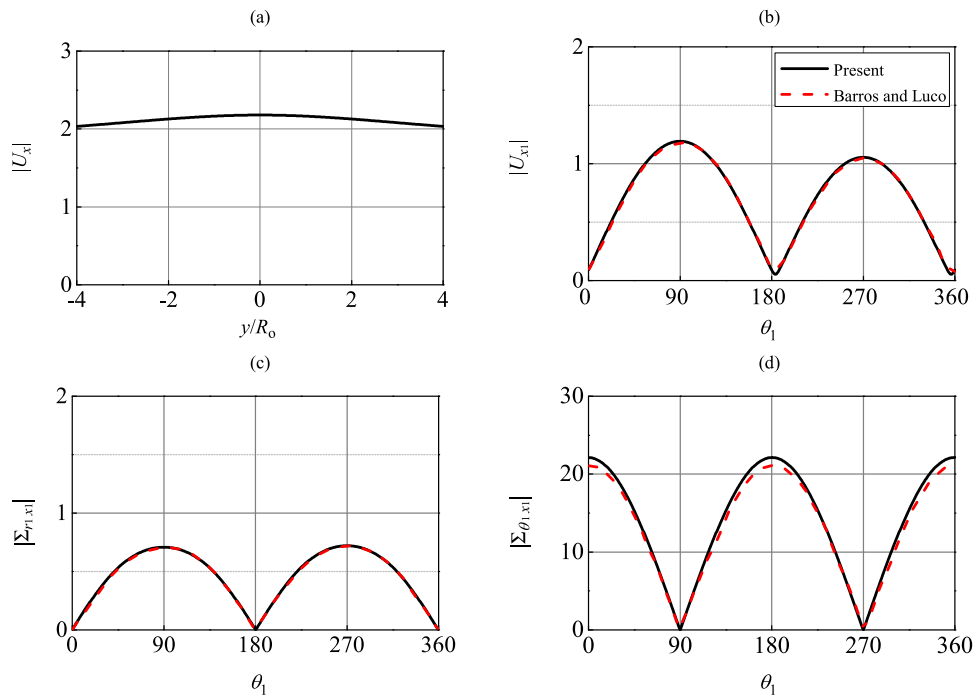
Fig. 7. The third comparison example for the 2D SH wave case ($\chi_{inc}^{(1)}$): (a) U_x at $z = 0$, (b) U_{x_1} at $r_1 = R_o$, (c) $\Sigma_{r_1 x_1}$ at $r_1 = R_o$ and (d) $\Sigma_{\theta_1 x_1}$ at $r_1 = R_i$. The excitation is a vertically incident SH wave ($\theta_v = 0°$ and $\theta_h = 90°$), and the first parameter set in Table 1 is used. Note that for panel (a) no result from literature is available.

7.2. 2D plane-strain cases

The comparison studies for the two-dimensional plane-strain cases consider the problem of a tunnel embedded in an elastic half-space subjected to incident P and SV waves (i.e., $\phi_{inc}^{(1)}$ and $\psi_{inc}^{(1)}$, respectively). We discuss three examples. First, we consider a case of vertically incident P and SV waves ($\theta_v = 0°$ and $\theta_h = 90°$) using the fourth parameter set in Table 1 and compare our results with the results obtained by Datta et al. [35]. Fig. 8(a) and (b) show the radial displacement U_{r_1} at the tunnel–soil interface $r_1 = R_o$ and the hoop stresses $\Sigma_{\theta_1 \theta_1}$ at the centre-line of the tunnel $r_1 = R_c$ for the incident P wave, while Fig. 8(d) and (e) show these quantities for the incident SV waves. It is clear that the results obtained by the present method are in good agreement with those in the literature.

For comparison, in Fig. 8(e), we added the results obtained by the present method using Hankel functions to represent the cylindrical waves in the tunnel (see Section 3.2), and small differences are observed compared with the literature results. Furthermore, we can verify that the results obtained using Hankel functions are not completely smooth; this is because the cylindrical wavenumbers in the tunnel are small (the combination of frequency and tunnel stiffness leads to $k_b^{(2)}$ ($= k_S^{(2)}$) being small), which makes that the corresponding Hankel functions become large. In this situation, the Hankel functions render the columns of matrix $\mathbf{K}$ (see Eq. (39)) linearly dependent given the limitation of the computer precision, which leads to an ill-conditioned system of equations and $\mathbf{K}$ having a large condition number (the results can be improved to some extent when quadruple precision is used (not standard in Matlab) in solving the system of equations). We see a similar non-smooth curve in the second 2D plane-strain example, Fig. 9(d), for which the cylindrical wavenumbers are even smaller. It can be verified that the non-smooth feature does not disappear even when large amounts of hysteretic damping are added in the system (results not shown). From Figs. 8(e) and 9(d), we observe that when Bessel functions are used instead of Hankel functions to represent the cylindrical waves in the tunnel, the method gives smooth and accurate results. The reason is that Bessel functions do not render the columns of matrix $\mathbf{K}$ linearly dependent, and therefore the problem

of limited precision is less severe with Bessel functions than with Hankel functions. As a result, the condition number of matrix $\mathbf{K}$ is effectively reduced when Bessel functions are used. We also found that the boundary conditions at the inner surface of the tunnel and the continuity conditions at the tunnel–soil interface are then satisfied much better.

In order to demonstrate that the literature result in Fig. 8 (as well as the present result) is correct, we also included the hoop stress (Fig. 8(e)) obtained by the indirect boundary element method (indirect BEM). Clearly, a perfect match with the literature result is observed. More details regarding our implementation of the indirect BEM can be found in Section 8.

We also present the displacements at the ground surface for the first example. Fig. 8(c) and (f) show that under the vertically incident P wave, the vertical displacement U_z is approximately equal to 2 (i.e., amplification factor is 2), while the horizontal displacement U_y is approximately equal to 0. On the contrary, for the vertically incident SV wave, the horizontal displacement $U_y \approx 2$ and $U_z \approx 0$. Therefore, the vertical and horizontal displacement components are the dominant displacement components for the incident P ($\phi_{inc}^{(1)}$) and SV ($\psi_{inc}^{(1)}$) waves, respectively. It can be verified that for a 3D problem the vertical, horizontal and longitudinal displacements (i.e., U_z, U_y and U_x) are the dominant displacement components for $\phi_{inc}^{(1)}$, $\psi_{inc}^{(1)}$ and $\chi_{inc}^{(1)}$, respectively. In Section 8, we study the effect of system parameters on the dominant displacement components at the ground surface for the three different incident wave types.

In the second example, the fifth parameter set in Table 1 is used. The ratio of the tunnel depth to its inner radius ($H/R_i = 2.0$) is smaller than that in the first example ($H/R_i = 8.33$), and we consider a non-vertically incident wave case ($\theta_v = 10°$ and $\theta_h = 90°$). Fig. 9 shows the response under the incident P and SV waves. We observe that the agreement with results from [25] is very good but $\Sigma_{\theta_1 \theta_1}$ is not smooth when Hankel functions are used to represent the waves in the tunnel, which is again related to the cylindrical wavenumbers in the tunnel being small. Clearly, the non-smoothness is more severe for the incident S wave case. Therefore, one may infer that the present method works better for the incident P wave case than the S wave case;
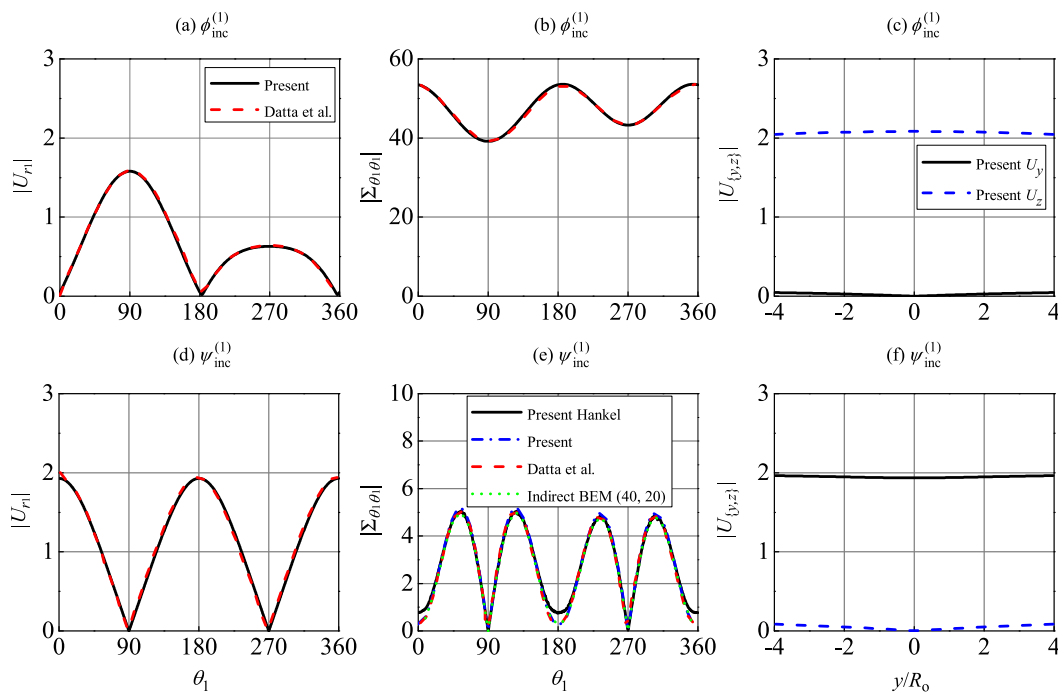
Fig. 8. The first comparison example for the 2D P-SV wave case ($\phi_{inc}^{(1)}$ and $\psi_{inc}^{(1)}$): (a), (d): U_{r_1} at $r_1 = R_o$; (b), (e): $\Sigma_{\theta_1 \theta_1}$ at $r_1 = R_c$; and (c), (f): $U_{\{y,z\}}$ at $z = 0$. The excitations are vertically incident P and SV waves ($\theta_v = 0°$ and $\theta_h = 90°$), respectively. The fourth parameter set in Table 1 is used. Note that for panels (c) and (f) no result from literature is available.

see also Section 8.1. However, that is not necessarily true, as shown in Section 8.2, where the influence of the stiffness contrast is investigated in more detail. In addition, the non-smoothness of the response curves is more severe in the shallow tunnel case (see Fig. 9(d)) than the deep tunnel case (see Fig. 8(e)). This is confirmed by the analysis in Section 8.3.

It is shown in Fig. 9 that the distributions of the hoop stress $\Sigma_{\theta_1 \theta_1}$ and axial stress $\Sigma_{x_1 x_1}$ are very similar, though the amplification of the hoop stress is much higher than that of the axial stress. Fig. 9(c) and (f) show that the extremes of the radial and tangential displacements U_{r_1} and U_{θ_1} are both around 2, which is different from what we observed at the free surface, where there is one dominant displacement component (dependent on incident wave type). However, we do see that the radial displacement U_{r_1} has maxima where the tangential displacement U_{θ_1} has minima, and vice versa.

In the third example, we consider a vertically incident wave case ($\theta_v = 0°$ and $\theta_h = 90°$), and use the first parameter set. The obtained results are shown in Fig. 10, where we observe a perfect match between the present results and those obtained by Liu et al. [13]. In this example, the stiffness ratio of the tunnel to soil is small, and the tunnel is embedded at relatively large depth. Therefore, as opposed to the first two examples considered in this section, the results obtained when Hankel functions are used also match perfectly the literature results, but they are not shown in Fig. 10 for brevity. Fig. 10(c) and (f) show the normal radial stress $\Sigma_{r_1 r_1}$ and shear stress $\Sigma_{r_1 \theta_1}$ for the vertically incident P and SV waves, respectively. We see that the distributions of $\Sigma_{r_1 r_1}$ and $\Sigma_{\theta_1 \theta_1}$ are the same, and the amplitude of $\Sigma_{r_1 r_1}$ does not exceed 1. Furthermore, we observe that the bending in the circumferential direction is more severe for the incident SV wave case than for the incident P wave case.

7.3. 3D case

One example of a 3D problem with incident P and S waves (i.e., $\phi_{inc}^{(1)}$ and $\chi_{inc}^{(1)}$, respectively) is given in this subsection. The first parameter set is used with obliquely incident P and S waves under incident angles $\theta_v = 30°$ and $\theta_h = 0°$. The obtained results are shown in Fig. 11,

where we observe excellent agreement between the present results and those obtained by Liu et al. [13]. Note that the results obtained using the indirect BEM are also included for this validation case, and good agreement is observed as well.

8. Accuracy of the present method and parametric studies

As shown in Section 7, the present method works very well when Bessel functions are used for the wave field in the tunnel. This is not necessarily the case when Hankel functions are used instead (i.e., when there is high stiffness contrast between the tunnel and soil, or when the tunnel is shallow; see Figs. 8 and 9). To gain more insight into the accuracy of the present method, we evaluate in this section the influence of five different parameters in the system: the dimensionless frequency, the stiffness ratio of the tunnel to soil, the embedded depth of the tunnel, the vertical incident wave angle and the thickness of the tunnel. Note that for the analysis in Sections 8.1, 8.3, 8.4 and 8.5, the results obtained when Hankel functions are used for the wave field in the tunnel are the same as the ones obtained using Bessel functions, but the former results are not shown for brevity.

To evaluate the accuracy of the present method, we also implemented the indirect BEM. The formulation of the indirect BEM for the current seismic wave problem is similar to the formulation for the moving-load problem [36], only the external force is different. The implementation of the indirect BEM for the seismic wave problem has been validated for each case, but only two cases are shown in this paper; see Figs. 8 and 11. To check the convergence of the indirect BEM, we considered different numbers of receiver and source points: $(N_r, N_s) = (40, 20)$ and $(N_r, N_s) = (80, 40)$. Figs. 12–16 show that $(N_r, N_s) = (40, 20)$ is sufficient for all the calculations in this paper. Note that we considered a very small amount of hysteretic material damping (i.e., material damping ratio being 0.001) in the implementation of the indirect BEM.

Throughout this section, we display the hoop stress at the centre-line of the tunnel and displacements at the ground surface. The hoop stress is chosen as it is the most important response component for the tunnel. For the ground vibrations, we choose the vertical, horizontal
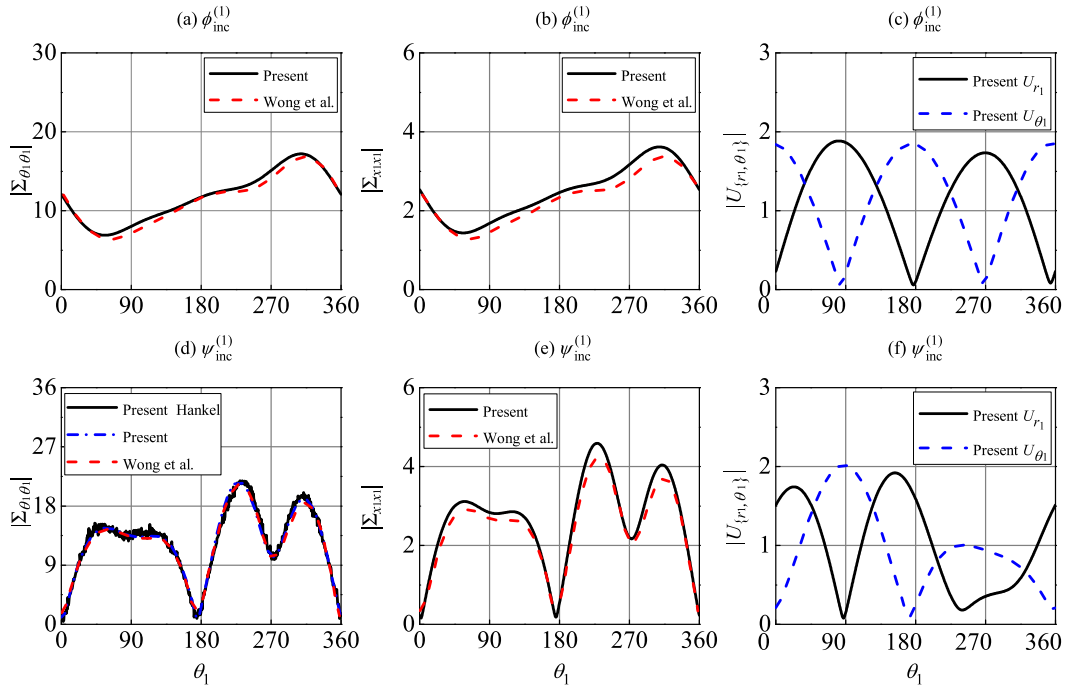
Fig. 9. The second comparison example for the 2D P-SV wave case ($\phi_{\text{inc}}^{(1)}$ and $\psi_{\text{inc}}^{(1)}$): (a), (d): $\Sigma_{\theta_1\theta_1}$ at $r_1 = R_c$; (b), (e): $\Sigma_{x_1x_1}$ at $r_1 = R_c$; and (c), (f): $U_{\{r_1,\theta_1\}}$ at $r_1 = R_o$. The excitations are non-vertically incident P and SV waves ($\theta_v = 10°$ and $\theta_h = 90°$), respectively. The fifth parameter set in Table 1 is used. Note that for panels (c) and (f) no result from literature is available.
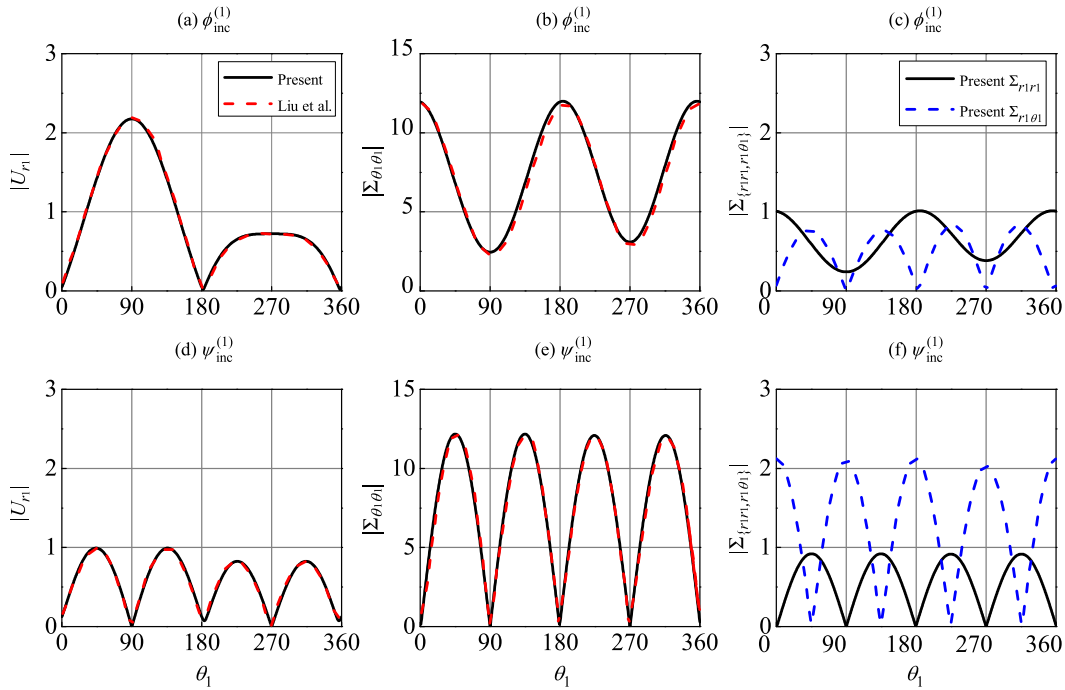
Fig. 10. The third comparison example for the 2D P-SV wave case ($\phi_{\text{inc}}^{(1)}$ and $\psi_{\text{inc}}^{(1)}$): (a), (d): U_{r_1} at $r_1 = R_o$; (b), (e): $\Sigma_{\theta_1\theta_1}$ at $r_1 = R_c$; and (c), (f): $\Sigma_{\{r_1r_1,r_1\theta_1\}}$ at $r_1 = R_o$. The excitations are vertically incident P and SV waves ($\theta_v = 0°$ and $\theta_h = 90°$), respectively. The first parameter set in Table 1 is used. Note that for panels (c) and (f) no result from literature is available.

and longitudinal displacements U_z, U_y and U_x for $\phi_{\text{inc}}^{(1)}$, $\psi_{\text{inc}}^{(1)}$ and $\chi_{\text{inc}}^{(1)}$, respectively, as they are the dominant displacement components; see Section 7.2. The first parameter set in Table 1, and $\theta_v = 30°$ and $\theta_h = 0°$ are used as the base case in the following analysis. We display the maximum of the absolute value of hoop stresses around the tunnel, and the maximum of the absolute value of ground vibrations in the range of

$y/R_o = [-4, 4]$. Furthermore, the effects of the five different parameters on the response of the system are briefly discussed as well.

8.1. Dimensionless frequency

As seismic waves typically have low frequencies, we consider the dimensionless frequency in the range of $0.002 - 1.5$ ($\tilde{f} = 0.2 - 154.8$ Hz).
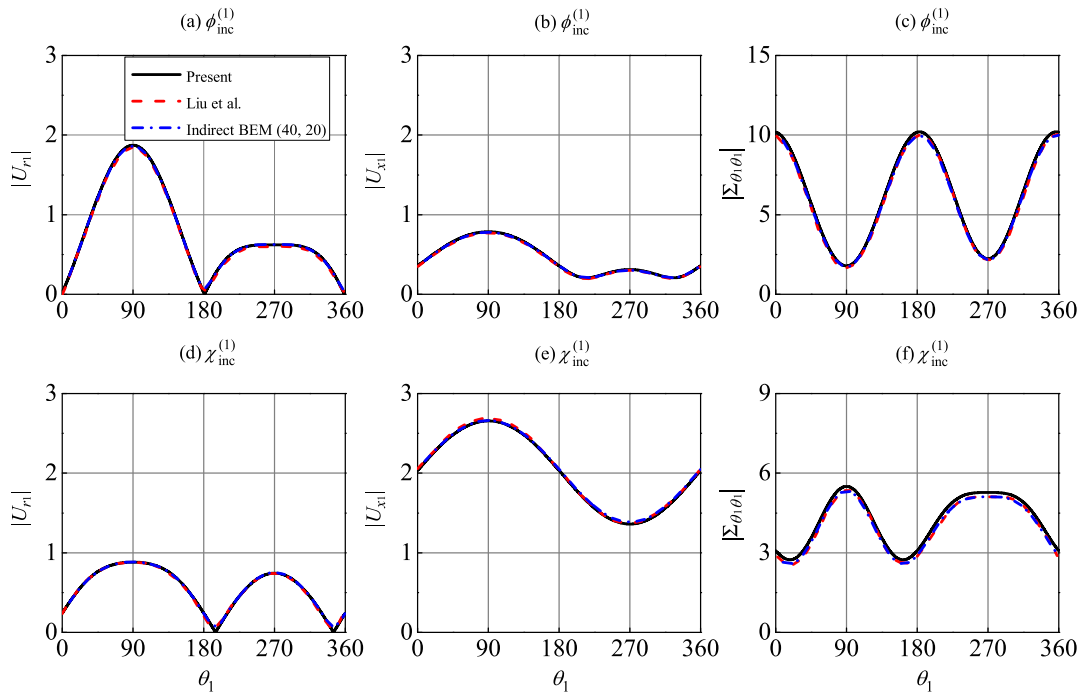
Fig. 11. An example for the 3D case ($\phi^{(1)}_{inc}$ and $\chi^{(1)}_{inc}$): (a), (d): U_{r_1} at $r_1 = R_o$; (b), (e): U_{x_1} at $r_1 = R_o$; and (c), (f): $\Sigma_{\theta_1\theta_1}$ at $r_1 = R_c$. The excitations are non-vertically incident P and S waves ($\theta_v = 30°$ and $\theta_h = 0°$), respectively. The first parameter set in Table 1 is used.
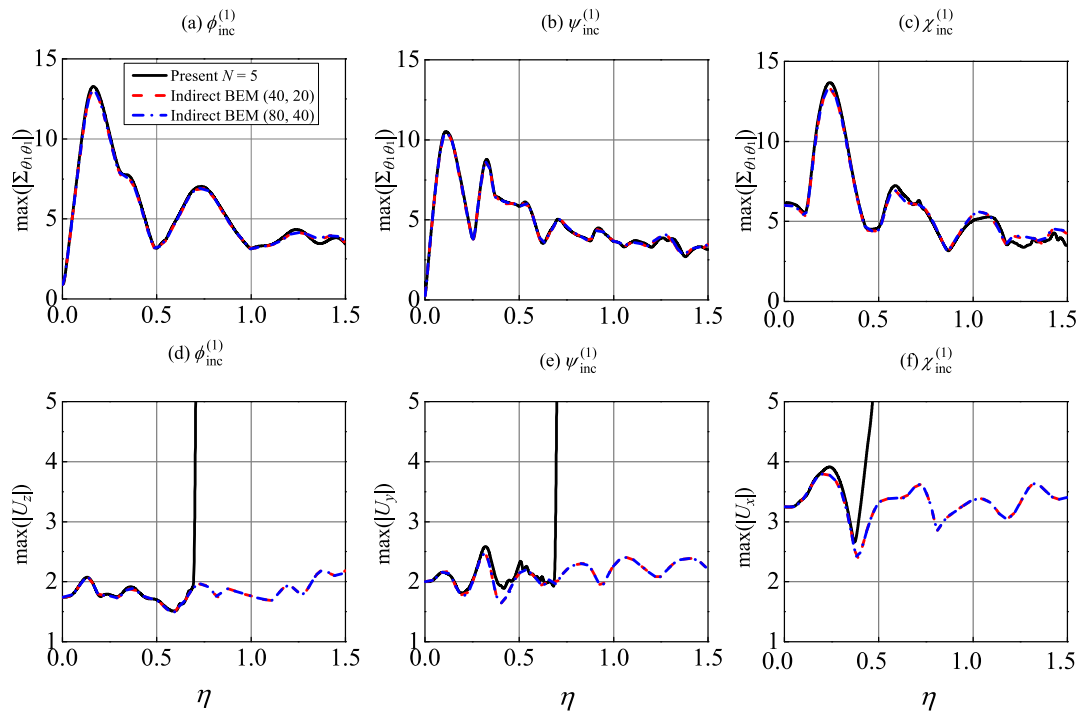
Fig. 12. Evaluation of the present method for the dimensionless frequency η: (a)–(c) hoop stress $\Sigma_{\theta_1\theta_1}$ at $r_1 = R_c$; (d)–(f) vertical displacement U_z, horizontal displacement U_y and longitudinal displacement U_x at $z = 0$ subject to $\phi^{(1)}_{inc}$, $\psi^{(1)}_{inc}$ and $\chi^{(1)}_{inc}$, respectively.

Fig. 12(a)–(c) show that the present method works well in terms of the hoop stress. Fig. 12(d)–(f) show that the present method also works well in terms of the ground vibrations for dimensionless frequencies up to 0.7, 0.69 and 0.46 ($\tilde{f}$ = 72.3, 71.2 and 47.5 Hz) under $\phi^{(1)}_{inc}$ and $\psi^{(1)}_{inc}$, and $\chi^{(1)}_{inc}$, respectively. Clearly, the method performs well for the frequency band of seismic waves. We included the higher frequencies in view of the applicability of the method for other, higher-frequency loadings.

For high dimensionless frequencies, the condition number of the formulated matrix **K** is very large, and the matrix equation Eq. (39) cannot be solved accurately. From the numerical analysis, we found that the boundary conditions at the inner surface of the tunnel and continuity conditions at the interface are still satisfied well for high frequencies, but the boundary conditions at the ground surface are not. Results are thus only accurate at the tunnel surfaces, not at the ground surface. The reason for the inaccuracy lies in the fact that the secondary

Fig. 13. Evaluation of the present method for the stiffness ratio of the tunnel to soil $E^{(2)}/E^{(1)}$: (a)–(c) hoop stress $\Sigma_{\theta_1\theta_1}$ at $r_1 = R_c$; (d)–(f) vertical displacement U_z, horizontal displacement U_y and longitudinal displacement U_x at $z = 0$ subject to $\phi_{\mathrm{inc}}^{(1)}$, $\psi_{\mathrm{inc}}^{(1)}$ and $\chi_{\mathrm{inc}}^{(1)}$, respectively.

scattered waves in the soil are represented by cylindrical waves and not plane waves, while the latter are most likely more suitable to represent the response at the flat ground surface at high frequencies. Using more circumferential modes does not help increasing accuracy; on the contrary, we can verify that the condition number gets larger, so the results obtained using more modes can be even worse. In fact, it is difficult to get converged results using the present method for high-frequency cases.

We observe that the present method generally works better for the incident P wave case ($\phi_{\mathrm{inc}}^{(1)}$) than the incident S wave case ($\psi_{\mathrm{inc}}^{(1)}$ and $\chi_{\mathrm{inc}}^{(1)}$); see also Fig. 9. The reason is that, for the incident S wave case, the longitudinal wavenumber $k_x^{(1)}$ is larger than that for the case of the incident P wave under the same frequency, as the speed of the S wave is smaller than that of the P wave. Thus, $k_a^{(1)}$ is smaller, which eventually results in a higher condition number of matrix **K** and less accurate responses; see explanation in Section 7.2, although the inaccuracy in this case originates from the Hankel functions in the soil, which cannot be replaced by Bessel functions as there are only outgoing waves.

Fig. 12 shows that for different incident wave types, the hoop stress has a dominant peak value at low frequencies, oscillates as frequency increases, and has a decreasing trend. The first two dimensionless resonance frequencies under $\phi_{\mathrm{inc}}^{(1)}$ are 0.15 and 0.74, respectively, under $\psi_{\mathrm{inc}}^{(1)}$ 0.11 and 0.33, and under $\chi_{\mathrm{inc}}^{(1)}$ 0.24 and 0.59. We also see that the curve for the incident S wave case oscillates more. In addition, as opposed to the decreasing trend for the hoop stress, the curves for ground vibrations exhibit a slightly increasing trend.

To conclude, the advantage of the proposed semi-analytical method is that it is very efficient regarding computational time. However, the condition number increases as frequency increases, which may lead to an increase in computational time (still efficient compared with indirect BEM) and, at some point, to inaccurate results. Thus, for seismic wave excitations, the semi-analytical method is beneficial, but its accuracy is lost for high-frequency loadings.

8.2. Stiffness ratio of the tunnel to soil

As mentioned in Section 7.2, the large stiffness contrast ($E^{(2)}/E^{(1)} = 23$) between the tunnel and soil may induce inaccuracies in the results

obtained by the present method when using Hankel functions to represent the cylindrical waves in the tunnel. Therefore, we evaluate it for varying stiffness ratio: $E^{(2)}/E^{(1)} = [0.5 - 25]$. The corresponding range for shear wave velocity in the soil is $C_S^{(1)} = [2123 \text{ m/s} - 300 \text{ m/s}]$ based on the shear velocity $C_S^{(2)} = 1725$ m/s. In this section, we show the results obtained by the present method using both Bessel and Hankel functions in Fig. 13. It is shown that the present method using Bessel functions works well for both the incident P and S waves in the complete considered range. However, regarding the hoop stress, the present method using Hankel functions does not give accurate results in the stiffness ratio range of $10 - 15$ for the incident P wave case. This improvement was already touched upon in Section 7.2.

The large stiffness contrast causes only a small inaccuracy in the results (i.e., the small difference in trend as the stiffness ratio increases); they are still satisfactory. Therefore, a large stiffness ratio does not necessarily lead to inaccurate results. It is surprising to see that the results are actually least accurate for a moderate stiffness contrast (range $10 - 15$), and for the incident P wave case. This is different from what we observed in Section 8.1 (and in Sections 8.3–8.5), where the present method seemed to perform better for the incident P than the incident S wave case.

To understand the inaccuracy in the range of $10 - 15$ for the incident P wave case, we consider the wavenumbers of refracted waves in the tunnel. One can verify that $k_b^{(2)}$ (see Eq. (24)) becomes imaginary when $E^{(2)}/E^{(1)} = 12.5$, which implies that the refracted shear wave becomes evanescent; $|k_b^{(2)}|$ is small in the interval of $E^{(2)}/E^{(1)} = [10 - 15]$, and $|k_b^{(2)}|$ is the smallest when $E^{(2)}/E^{(1)} = 12$. As explained in Section 7.2, the small argument of a Hankel function results in inaccurate responses (it can be verified that the inaccuracy does not completely disappear when large amounts of hysteretic damping are added in the system). That is the reason why the responses are inaccurate for $E^{(2)}/E^{(1)} = [10 - 15]$, and why the largest discrepancy occurs when $E^{(2)}/E^{(1)} = 12$. Similarly, the (small) inaccuracy observed for the incident S wave case (see Fig. 13(c) and (e)) when $E^{(2)}/E^{(1)} = 3$ is again caused by the refracted S wave becoming evanescent, and $k_b^{(2)}$ being the smallest for this stiffness contrast. Fortunately, when Bessel functions are used,

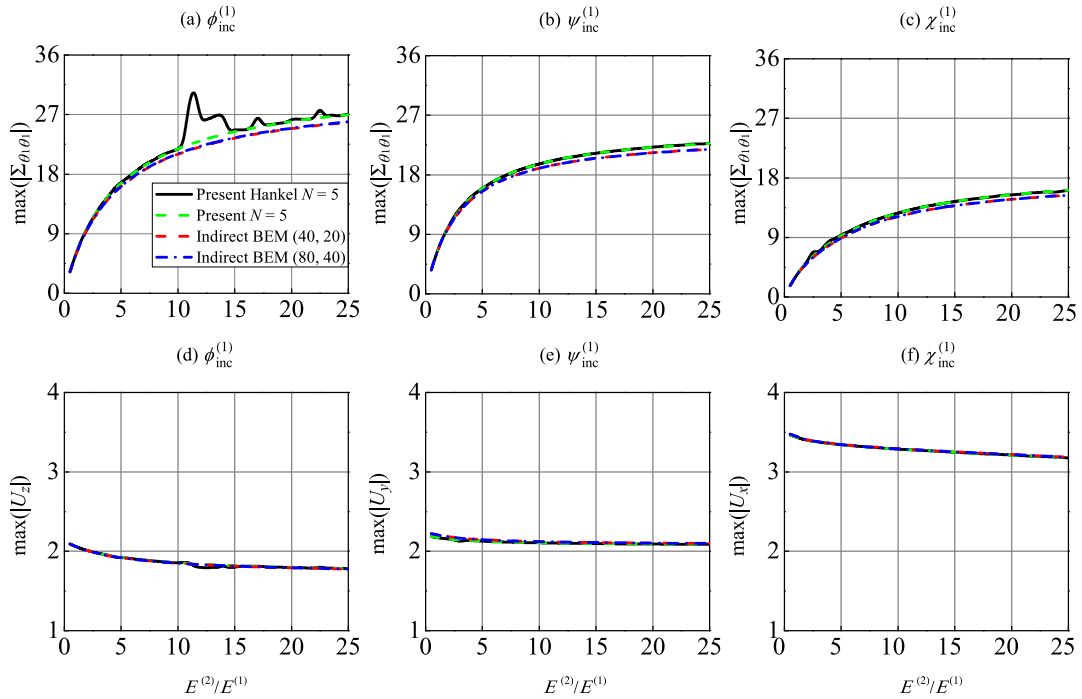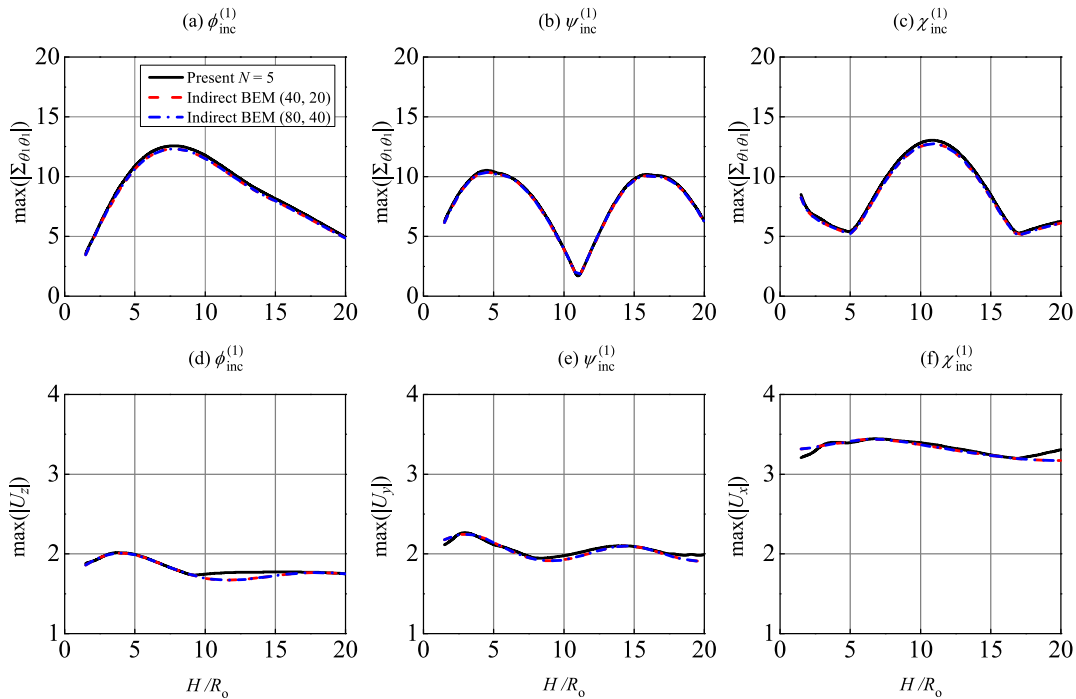**Fig. 14.** Evaluation of the present method for the depth ratio H/R_o: (a)–(c) hoop stress $\Sigma_{\theta_1\theta_1}$ at $r_1 = R_c$; (d)–(f) vertical displacement U_z, horizontal displacement U_y and longitudinal displacement U_x at $z = 0$ subject to $\phi_{inc}^{(1)}$, $\psi_{inc}^{(1)}$ and $\chi_{inc}^{(1)}$, respectively.

the condition number of matrix **K** is effectively reduced and accurate results can be obtained for the small wavenumbers.

Fig. 13 shows that the hoop stress increases dramatically as the stiffness ratio increases, which indicates that the hoop stress in the tunnel can be reduced effectively by replacing the surrounding soft soil by stiff soil (i.e., by means of ground improvement). The hoop stress under $\phi_{inc}^{(1)}$ is the largest, and the one under $\chi_{inc}^{(1)}$ is the smallest. It is also shown that the ground vibrations decrease only slightly as the stiffness ratio increases.

8.3. Embedded depth of the tunnel

In this section, we evaluate the present method for the embedded depth of the tunnel, and the considered range of embedded depth ratio is that $H/R_o = [1.5 - 20]$. The results are shown in Fig. 14. We observe that the present method works very well in general for both the P and S wave cases, despite some small differences between the current results and those obtained using the indirect BEM. The reason why the present method works less good for shallow tunnels with $H/R_o = [1.5 - 2]$ (see Fig. 14(e) and (f)) is that the wavenumbers are small in this range.

Fig. 14(d)–(f) show that the ground vibrations at the ground surface have a decreasing trend. The ground vibrations are amplified more for shallow tunnels due to 'trapped' waves between the top of the tunnel and the ground surface [16,17]. We observe in Fig. 14(a)–(c) that the embedded depth has a large effect on the hoop stress, for all three incident wave types. Both the distributions and magnitudes of the hoop stress are different, and the peak values occur at different depth ratios. In addition, we see that the response (both the hoop stress and ground vibration) for the incident P wave is not always larger than that for the incident S wave, which is different from what is claimed in [16] that generally greater amplifications are observed for P waves than for SV waves. For example, the hoop stress under $\phi_{inc}^{(1)}$ is the largest when $H/R_o = [5 - 9.25]$; the hoop stress under $\psi_{inc}^{(1)}$ is the largest when $H/R_o = [2 - 5, 14.5 - 20]$; the hoop stress under $\chi_{inc}^{(1)}$ is the largest when $H/R_o = [9.25 - 14.5]$. Therefore, a larger embedded depth does not necessarily make the tunnel safer. In fact, we can verify that the hoop stress shows a decreasing trend with increasing embedded depth, but

the decrease is not monotonic as quasi-periodic patterns appear. The ground displacements (Fig. 14(d)–(f)) show similar patterns, although the oscillation is less strong.

8.4. Vertical incident angle

Here, we evaluate the present method for the vertical incident angle θ_v, while we consider $\theta_h = 0°$. Note that for the considered soil parameter set with $v^{(1)} = 0.333$, $\theta_v^{crit} = \arcsin\left(\sqrt{\left(1 - 2v^{(1)}\right)/\left(2 - 2v^{(1)}\right)}\right) \approx 30°$ for the incident S wave case (see Eq. (19)). Fig. 15 shows that the results obtained by the present method are accurate for both the incident P and S wave cases. Note that the scattered compressional waves in the soil become evanescent (i.e., $k_a^{(1)}$ becomes imaginary) when $\theta_v \approx 30°$ (see Eqs. (15), (19) and (22); as we consider $\theta_h = 0°$, $k_y^{(1)} = 0$ and $k_a^{(1)} = k_{z,P}^{(1)}$). As explained in Section 8.2, we expect inaccuracy at the transition to evanescent waves. One can verify that the obtained results are indeed less accurate around $\theta_v = 30°$ especially when using $N = 10$; however, the obtained results using $N = 5$ are satisfactory. Therefore, the inaccuracy issue regarding the angle (i.e., scattered compressional waves becoming evanescent) is less severe than in the case of unfavourable stiffness ratio (i.e., refracted shear waves becoming evanescent). In addition, this suggests that it is not recommendable to use more than necessary circumferential modes in the computations.

Fig. 15(a) and (b) show that the hoop stress decreases significantly as θ_v increases for the cases of $\phi_{inc}^{(1)}$ and $\psi_{inc}^{(1)}$; however, the hoop stress first increases and then decreases for the case of $\chi_{inc}^{(1)}$. We observe two small peaks at $\theta_v = 24.5°$ and $\theta_v = \theta_v^{crit} \approx 30°$, and a pronounced peak at $\theta_v = 39°$. Similar to the trend of the hoop stress, the dominant displacement U_z decreases under $\phi_{inc}^{(1)}$. However, the influence of θ_v on the dominant displacement U_y is very small. The dominant longitudinal displacement under $\chi_{inc}^{(1)}$ varies more as θ_v increases, and there is a pronounced peak at $\theta_v = \theta_v^{crit} \approx 30°$ and a second small peak at $\theta_v = 64°$. We can conclude that θ_v^{crit} has a large effect on the response of the system, especially under $\chi_{inc}^{(1)}$.
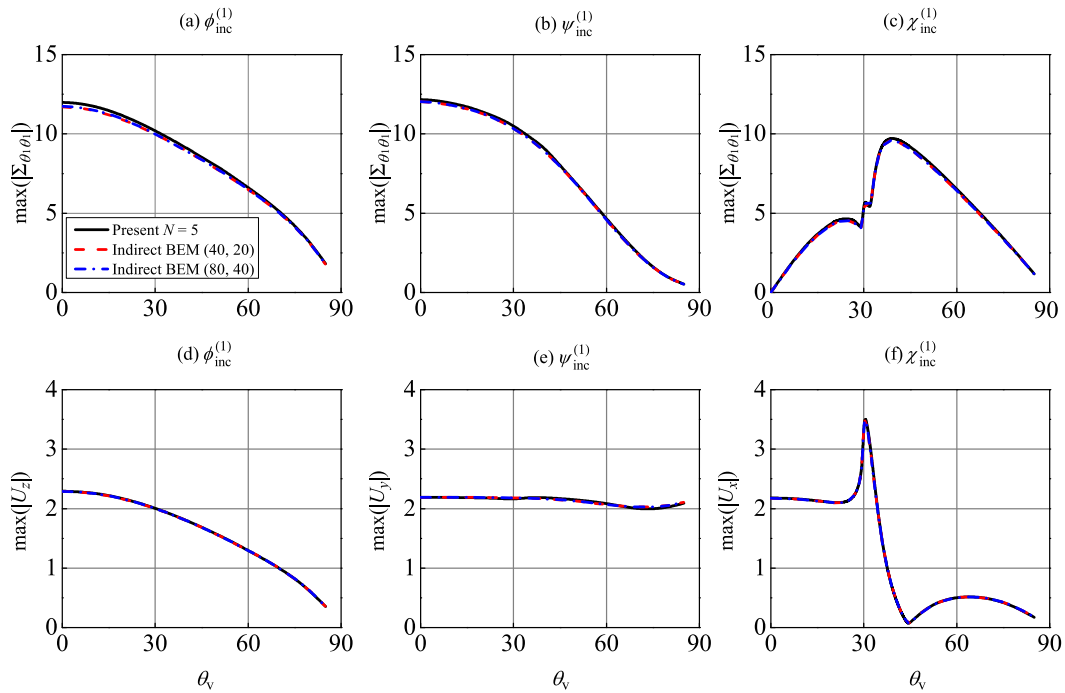
Fig. 15. Evaluation of the present method for the vertical incident angle θ_v: (a)–(c) hoop stress $\Sigma_{\theta_1\theta_1}$ at $r_1 = R_c$; (d)–(f) vertical displacement U_z, horizontal displacement U_y and longitudinal displacement U_x at $z = 0$ subject to $\phi_{inc}^{(1)}$, $\psi_{inc}^{(1)}$ and $\chi_{inc}^{(1)}$, respectively.
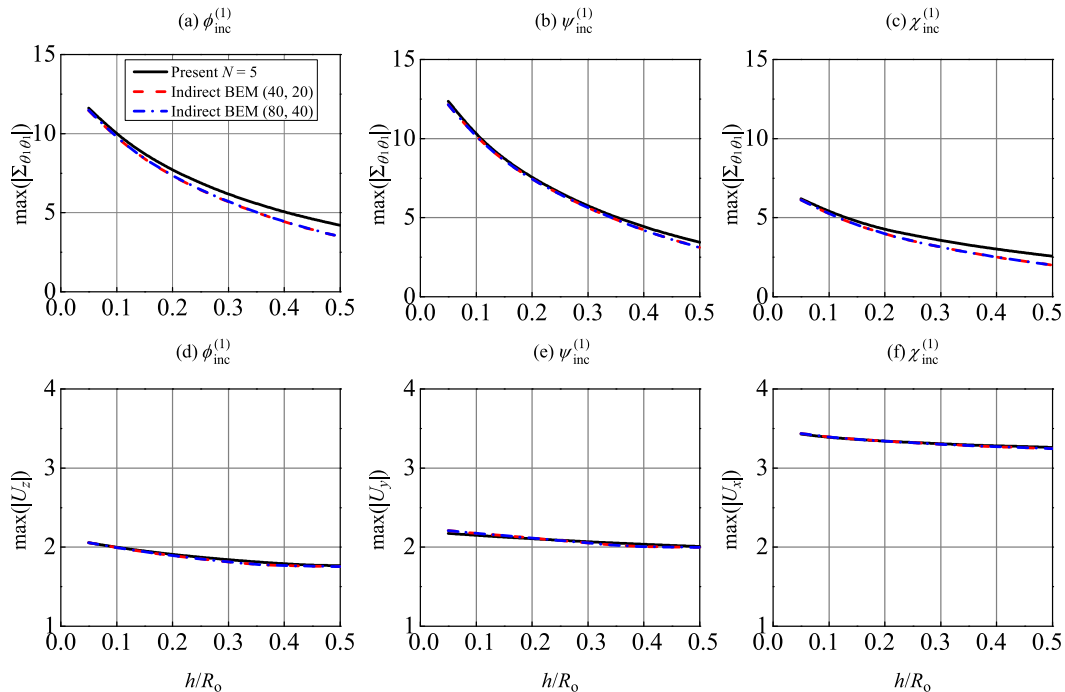
Fig. 16. Evaluation of the present method for the thickness ratio of the tunnel h/R_o: (a)–(c) hoop stress $\Sigma_{\theta_1\theta_1}$ at $r_1 = R_c$; (d)–(f) vertical displacement U_z, horizontal displacement U_y and longitudinal displacement U_x at $z = 0$ subject to $\phi_{inc}^{(1)}$, $\psi_{inc}^{(1)}$ and $\chi_{inc}^{(1)}$, respectively.

8.5. Thickness of the tunnel

The evaluation of the present method for changing thickness ratio h/R_o is presented in this section. We consider a range of $0.05 - 0.5$. Fig. 16 shows that the present method works well for both the incident P and S wave cases. The reason why the (small) difference between the results obtained using the present method and those using the indirect BEM increases as the thickness ratio increases, is that the tunnel is

modelled by the Flügge shell theory in the indirect BEM, while the tunnel is modelled as an elastic continuum in the current method.

Fig. 16(a)–(c) show that the hoop stress decreases significantly as the thickness of the tunnel increases. This suggest that a thicker tunnel is indeed safer. Furthermore, the hoop stress under $\phi_{inc}^{(1)}$ and $\psi_{inc}^{(1)}$ is much larger than that under $\chi_{inc}^{(1)}$. Fig. 16(d)–(f) show that all the dominant displacement components decrease slightly as the thickness of the tunnel increases. Different from what we observed for the hoop

stress, the dominant displacement under $\chi_{\text{inc}}^{(1)}$ is much larger than that under $\phi_{\text{inc}}^{(1)}$ and $\psi_{\text{inc}}^{(1)}$.

9. Conclusions

A semi-analytical solution for the 3D response of a tunnel embedded in an elastic half-space subject to seismic waves has been presented in this paper. An existing method has been extended successfully from 2D to 3D. Both the tunnel and soil were modelled as an elastic continuum. The method of conformal mapping (which employs the complex-variable theory) was used to map the original physical domain with boundary surfaces of two different types onto an image domain with boundary surfaces of the same type. The total wave field in the soil consists of incident and reflected plane waves, and directly and secondary scattered cylindrical waves, while the total wave field in the tunnel only consists of refracted cylindrical waves. The secondary scattered waves are generated when the cylindrical waves directly scattered from the tunnel meet the half-space surface. They were represented by cylindrical waves that originate from a source of a priori unknown intensity located at the centre of the image of the tunnel, which is positioned symmetrically with respect to the half-space surface.

The unknown coefficients of the potentials related to the cylindrical waves were determined by the boundary and continuity conditions of the tunnel–soil system. The boundary value problem was solved in the image domain from a system of algebraic equations obtained by projecting the boundary and continuity conditions onto the set of the circumferential basis functions/modes. Convergence tests were conducted regarding the number of circumferential modes (N), and it was shown that $N = 5$ appears sufficient for the considered scenarios in this paper. The results obtained by the present method were validated for 2D anti-plane, 2D plane-strain and 3D cases by literature results. Excellent agreement was observed.

The performance of the present solution method has been systematically evaluated and the effect of five important parameters on the response of the system has been addressed briefly as well. The main findings are as follows:

- The present method performs well for the frequency band of seismic waves. For high dimensionless frequencies, the condition number of the formulated matrix obtained from the boundary and continuity conditions is very high, which causes inaccurate results. The proposed method generally works better for the incident P wave case than the incident S wave case. The reason is that the wavenumbers in the arguments of the Hankel functions (representing the cylindrical waves in the soil) are small, implying that the Hankel functions render the columns of matrix **K** linearly dependent for the S wave case, which eventually results in ill-conditioned system of equations and less accurate responses. The hoop stress decreases as frequency increases in a global sense, while the dominant displacement component increases as frequency increases. Furthermore, the results reveal pronounced resonances which should be avoided in the design of tunnels.
- In the considered range of the stiffness ratio of the tunnel to soil, the proposed method works well in general when Bessel functions are used to represent the cylindrical waves in the tunnel. In contrast, when Hankel functions are used to represent waves in the tunnel, the hoop stress becomes inaccurate for a stiffness ratio in the range of $10 - 15$. The reason is that the wavenumbers in the Hankel functions (representing the cylindrical waves in tunnel) are small in this moderate stiffness contrast range, which is due to refracted shear waves (in the tunnel) becoming evanescent (in the 3D case). These inaccuracies can be perfectly overcome by representing the cylindrical waves in the tunnel by Bessel functions.
  The hoop stress increases dramatically as the stiffness ratio of the tunnel to soil increases, which indicates that the hoop stress in the

tunnel can be reduced effectively by replacing the surrounding soft soil by stiff soil, while the ground vibrations decrease slightly as the soil stiffness decreases.

- The present method generally works well in the considered range of the embedded depth of the tunnel.
  It is shown that the hoop stress has a peak value at different embedded depths for three different incident waves (P wave and two differently polarised S waves), and the ground vibrations are amplified more for shallow tunnels. A larger embedded depth does not necessarily make the tunnel safer. The hoop stress shows a decreasing trend with increasing embedded depth, but the decrease is not monotonic as quasi-periodic patterns appear. The ground displacements show similar patterns, although the oscillation is less strong.
- The present method generally works well in the considered range of the vertical incident angle.
  The vertical incident angle has a large effect on the response of the system. The hoop stress decreases significantly as the vertical incident angle increases for $\phi_{\text{inc}}^{(1)}$ (P wave) and $\psi_{\text{inc}}^{(1)}$ (S wave), while the hoop stress for $\chi_{\text{inc}}^{(1)}$ (different S wave) first increases and then decreases, with a pronounced peak value where the vertical incident angle is slightly larger than the critical vertical incident angle. The dominant ground vibration decreases as the vertical incident angle increases for $\phi_{\text{inc}}^{(1)}$; the dominant ground vibration does not change much for $\psi_{\text{inc}}^{(1)}$, while there is a pronounced peak at the critical vertical incident angle for $\chi_{\text{inc}}^{(1)}$.
- The present method generally works well in the considered thickness range of the tunnel.
  The hoop stress decreases significantly as the thickness of the tunnel increases, while the dominant ground vibrations decrease only slightly. This suggest that a thicker tunnel is indeed safer, and it is also somewhat beneficial for structures on the ground surface.

Finally, we can conclude that the proposed method is in general a fast, elegant and accurate method for solving the seismic wave scattering problem, and can be used for preliminary design.

Declaration of competing interest

The authors declare that they have no known competing financial interests or personal relationships that could have appeared to influence the work reported in this paper.

Data availability

The data that has been used is confidential.

Appendix A. Amplitude ratios of potentials of reflected to incident plane waves

Amplitude ratios of potentials of reflected waves to incident plane waves in a homogeneous half-space without embedded structures can be determined based on the stress-free boundary conditions at the half-space surface. The result is presented in this appendix.

Case 1: Incident compressional wave ($\phi_{\text{inc}}^{(1)}$). The amplitude ratios ($R_{\phi,\phi}$, $R_{\psi,\phi}$ and $R_{\chi,\phi}$) of the reflected waves ($\phi_{\text{ref}}^{(1)}$, $\psi_{\text{ref}}^{(1)}$ and $\chi_{\text{ref}}^{(1)}$) to incident wave ($\phi_{\text{inc}}^{(1)}$) are given as follows:

$$R_{\phi,\phi} = \frac{4k_{z,\text{P}}k_{z,\text{S}}k^2 - \left(2k^2 - k_{\text{S}}^2\right)^2}{4k_{z,\text{P}}k_{z,\text{S}}k^2 + \left(2k^2 - k_{\text{S}}^2\right)^2}, \quad R_{\psi,\phi} = \frac{4k_{z,\text{P}}k_y\left(2k^2 - k_{\text{S}}^2\right)\left(k_{\text{S}}/k_{\text{b}}\right)^2}{4k_{z,\text{P}}k_{z,\text{S}}k^2 + \left(2k^2 - k_{\text{S}}^2\right)^2},$$

$$R_{\chi,\phi} = \frac{4\,\mathrm{i}\,k_{z,\mathrm{P}}k_{z,\mathrm{S}}k_x k_{\mathrm{S}}\left(2k^2 - k_{\mathrm{S}}^2\right)/k_{\mathrm{b}}^2}{4k_{z,\mathrm{P}}k_{z,\mathrm{S}}k^2 + \left(2k^2 - k_{\mathrm{S}}^2\right)^2}, \tag{A.1}$$

where the first and second subscripts indicate the potentials of the reflected and incident waves, respectively. It is understood that all the wavenumbers shown in this section are associated with the soil medium and should have the superscript "(1)". However, this superscript is omitted for brevity. For example, $k = k^{(1)}$, as defined in Eq. (16).

Note that when the axial wavenumber k_x equals to zero, a 2D problem is recovered. Consequently, we have $k = k_y$, $k_{\mathrm{S}} = k_{\mathrm{b}}$, and the amplitude ratios shown in Eq. (A.1) are reduced to the following expressions:

$$R_{\phi,\phi} = \frac{4k_{z,\mathrm{P}}k_{z,\mathrm{S}}k^2 - \left(2k^2 - k_{\mathrm{S}}^2\right)^2}{4k_{z,\mathrm{P}}k_{z,\mathrm{S}}k^2 + \left(2k^2 - k_{\mathrm{S}}^2\right)^2},$$

$$R_{\psi,\phi} = \frac{4k_{z,\mathrm{P}}k_y\left(2k^2 - k_{\mathrm{S}}^2\right)}{4k_{z,\mathrm{P}}k_{z,\mathrm{S}}k^2 + \left(2k^2 - k_{\mathrm{S}}^2\right)^2}, \quad R_{\chi,\phi} = 0. \tag{A.2}$$

Case 2: Incident shear wave ($\psi_{\mathrm{inc}}^{(1)}$). The amplitude ratios ($R_{\phi,\psi}$, $R_{\psi,\psi}$ and $R_{\chi,\psi}$) of the reflected waves ($\phi_{\mathrm{ref}}^{(1)}$, $\psi_{\mathrm{ref}}^{(1)}$ and $\chi_{\mathrm{ref}}^{(1)}$) to incident wave ($\psi_{\mathrm{inc}}^{(1)}$) are given as follows:

$$R_{\phi,\psi} = \frac{-4k_{z,\mathrm{S}}k_y\left(2k^2 - k_{\mathrm{S}}^2\right)}{4k_{z,\mathrm{P}}k_{z,\mathrm{S}}k^2 + \left(2k^2 - k_{\mathrm{S}}^2\right)^2},$$

$$R_{\psi,\psi} = \frac{8k_{z,\mathrm{P}}k_{z,\mathrm{S}}k_y^2 k_{\mathrm{S}}^2/k_{\mathrm{b}}^2 - \left[4k_{z,\mathrm{P}}k_{z,\mathrm{S}}k^2 + \left(2k^2 - k_{\mathrm{S}}^2\right)^2\right]}{4k_{z,\mathrm{P}}k_{z,\mathrm{S}}k^2 + \left(2k^2 - k_{\mathrm{S}}^2\right)^2}, \tag{A.3}$$

$$R_{\chi,\psi} = \frac{8\,\mathrm{i}\,k_{z,\mathrm{P}}k_{z,\mathrm{S}}^2 k_{\mathrm{S}}k_y k_x/k_{\mathrm{b}}^2}{4k_{z,\mathrm{P}}k_{z,\mathrm{S}}k^2 + \left(2k^2 - k_{\mathrm{S}}^2\right)^2}.$$

For $k_x = 0$, we obtain the amplitude ratios for the 2D problem (P-SV or plane-strain problem):

$$R_{\phi,\psi} = \frac{-4k_{z,\mathrm{S}}k_y\left(2k^2 - k_{\mathrm{S}}^2\right)}{4k_{z,\mathrm{P}}k_{z,\mathrm{S}}k^2 + \left(2k^2 - k_{\mathrm{S}}^2\right)^2},$$

$$R_{\psi,\psi} = \frac{4k_{z,\mathrm{P}}k_{z,\mathrm{S}}k^2 - \left(2k^2 - k_{\mathrm{S}}^2\right)^2}{4k_{z,\mathrm{P}}k_{z,\mathrm{S}}k^2 + \left(2k^2 - k_{\mathrm{S}}^2\right)^2}, \quad R_{\chi,\psi} = 0. \tag{A.4}$$

Case 3: Incident shear wave ($\chi_{\mathrm{inc}}^{(1)}$). The amplitude ratios ($R_{\phi,\chi}$, $R_{\psi,\chi}$ and $R_{\chi,\chi}$) of the reflected waves ($\phi_{\mathrm{ref}}^{(1)}$, $\psi_{\mathrm{ref}}^{(1)}$ and $\chi_{\mathrm{ref}}^{(1)}$) to incident wave ($\chi_{\mathrm{inc}}^{(1)}$) are given as follows:

$$R_{\phi,\chi} = \frac{4\,\mathrm{i}\,k_x\left(2k^4 - 3k^2 k_{\mathrm{S}}^2 + k_{\mathrm{S}}^4\right)/k_{\mathrm{S}}}{4k_{z,\mathrm{P}}k_{z,\mathrm{S}}k^2 + \left(2k^2 - k_{\mathrm{S}}^2\right)^2},$$

$$R_{\psi,\chi} = \frac{8\,\mathrm{i}\,k_{z,\mathrm{P}}k_{z,\mathrm{S}}^2 k_{\mathrm{S}}k_y k_x/k_{\mathrm{b}}^2}{4k_{z,\mathrm{P}}k_{z,\mathrm{S}}k^2 + \left(2k^2 - k_{\mathrm{S}}^2\right)^2}, \tag{A.5}$$

$$R_{\chi,\chi} = \frac{8k_{z,\mathrm{P}}k_{z,\mathrm{S}}k_y^2 k_{\mathrm{S}}^2/k_{\mathrm{b}}^2 - \left[4k_{z,\mathrm{P}}k_{z,\mathrm{S}}k^2 - \left(2k^2 - k_{\mathrm{S}}^2\right)^2\right]}{4k_{z,\mathrm{P}}k_{z,\mathrm{S}}k^2 + \left(2k^2 - k_{\mathrm{S}}^2\right)^2}.$$

For $k_x = 0$, we obtain the amplitude ratios for the 2D problem (SH or anti-plane shear problem):

$$R_{\phi,\chi} = 0, \quad R_{\psi,\chi} = 0, \quad R_{\chi,\chi} = 1. \tag{A.6}$$

Appendix B. Expressions for displacements and stresses in terms of complex variables

The components of the displacements and stresses in Cartesian coordinates (y, z, x) expressed in terms of the complex variables κ and $\bar{\kappa}$ are as follows, where the superscript $(i = \{1, 2\})$ is omitted for brevity (throughout this appendix):

$$u_y = \left(\frac{\partial\phi}{\partial\kappa} + \frac{\partial\phi}{\partial\bar{\kappa}}\right) + \mathrm{i}\left(\frac{\partial\psi}{\partial\kappa} - \frac{\partial\psi}{\partial\bar{\kappa}}\right) - \frac{\mathrm{i}\,k_x}{k_{\mathrm{S}}}\left(\frac{\partial\chi}{\partial\kappa} + \frac{\partial\chi}{\partial\bar{\kappa}}\right), \tag{B.1}$$

$$u_z = \mathrm{i}\left(\frac{\partial\phi}{\partial\kappa} - \frac{\partial\phi}{\partial\bar{\kappa}}\right) - \left(\frac{\partial\psi}{\partial\kappa} + \frac{\partial\psi}{\partial\bar{\kappa}}\right) + \frac{k_x}{k_{\mathrm{S}}}\left(\frac{\partial\chi}{\partial\kappa} - \frac{\partial\chi}{\partial\bar{\kappa}}\right), \tag{B.2}$$

$$u_x = -\mathrm{i}\,k_x\phi + \frac{k_{\mathrm{b}}^2}{k_{\mathrm{S}}}\chi, \tag{B.3}$$

and

$$\sigma_{yy} = -\lambda k_x^2\phi - (\lambda + \mu)\,k_{\mathrm{a}}^2\phi + 2\mu\left(\frac{\partial^2\phi}{\partial\kappa^2} + \frac{\partial^2\phi}{\partial\bar{\kappa}^2}\right) + 2\,\mathrm{i}\,\mu\left(\frac{\partial^2\psi}{\partial\kappa^2} - \frac{\partial^2\psi}{\partial\bar{\kappa}^2}\right)$$
$$+ \frac{\mathrm{i}\,\mu k_x k_{\mathrm{b}}^2}{k_{\mathrm{S}}}\chi - \frac{2\,\mathrm{i}\,\mu k_x}{k_{\mathrm{S}}}\left(\frac{\partial^2\chi}{\partial\kappa^2} + \frac{\partial^2\chi}{\partial\bar{\kappa}^2}\right), \tag{B.4}$$

$$\sigma_{zz} = -\lambda k_x^2\phi - (\lambda + \mu)\,k_{\mathrm{a}}^2\phi - 2\mu\left(\frac{\partial^2\phi}{\partial\kappa^2} + \frac{\partial^2\phi}{\partial\bar{\kappa}^2}\right) - 2\,\mathrm{i}\,\mu\left(\frac{\partial^2\psi}{\partial\kappa^2} - \frac{\partial^2\psi}{\partial\bar{\kappa}^2}\right)$$
$$+ \frac{\mathrm{i}\,\mu k_x k_{\mathrm{b}}^2}{k_{\mathrm{S}}}\chi + \frac{2\,\mathrm{i}\,\mu k_x}{k_{\mathrm{S}}}\left(\frac{\partial^2\chi}{\partial\kappa^2} + \frac{\partial^2\chi}{\partial\bar{\kappa}^2}\right), \tag{B.5}$$

$$\sigma_{xx} = -(\lambda + 2\mu)\,k_x^2\phi - \lambda k_{\mathrm{a}}^2\phi - \frac{2\,\mathrm{i}\,\mu k_x k_{\mathrm{b}}^2}{k_{\mathrm{S}}}\chi, \tag{B.6}$$

$$\sigma_{yz} = 2\,\mathrm{i}\,\mu\left(\frac{\partial^2\phi}{\partial\kappa^2} - \frac{\partial^2\phi}{\partial\bar{\kappa}^2}\right) - 2\mu\left(\frac{\partial^2\psi}{\partial\kappa^2} + \frac{\partial^2\psi}{\partial\bar{\kappa}^2}\right) + \frac{2\mu k_x}{k_{\mathrm{S}}}\left(\frac{\partial^2\chi}{\partial\kappa^2} - \frac{\partial^2\chi}{\partial\bar{\kappa}^2}\right), \tag{B.7}$$

$$\sigma_{yx} = -2\,\mathrm{i}\,\mu k_x\left(\frac{\partial\phi}{\partial\kappa} + \frac{\partial\phi}{\partial\bar{\kappa}}\right)$$
$$+ \mu k_x\left(\frac{\partial\psi}{\partial\kappa} - \frac{\partial\psi}{\partial\bar{\kappa}}\right) + \frac{\mu\left(k_{\mathrm{S}}^2 - 2k_x^2\right)}{k_{\mathrm{S}}}\left(\frac{\partial\chi}{\partial\kappa} + \frac{\partial\chi}{\partial\bar{\kappa}}\right), \tag{B.8}$$

$$\sigma_{zx} = 2\mu k_x\left(\frac{\partial\phi}{\partial\kappa} - \frac{\partial\phi}{\partial\bar{\kappa}}\right) + \mathrm{i}\,\mu k_x\left(\frac{\partial\psi}{\partial\kappa} + \frac{\partial\psi}{\partial\bar{\kappa}}\right)$$
$$+ \frac{\mathrm{i}\,\mu\left(k_{\mathrm{S}}^2 - 2k_x^2\right)}{k_{\mathrm{S}}}\left(\frac{\partial\chi}{\partial\kappa} - \frac{\partial\chi}{\partial\bar{\kappa}}\right). \tag{B.9}$$

Employing the transformation relations shown in Eqs. (11) and (12), the expressions for displacements and stresses in the cylindrical coordinate system (r, θ, x) are derived in terms of the complex variables κ and $\bar{\kappa}$:

$$u_r = \left(\mathrm{e}^{\mathrm{i}\theta}\frac{\partial\phi}{\partial\kappa} + \mathrm{e}^{-\mathrm{i}\theta}\frac{\partial\phi}{\partial\bar{\kappa}}\right) + \mathrm{i}\left(\mathrm{e}^{\mathrm{i}\theta}\frac{\partial\psi}{\partial\kappa} - \mathrm{e}^{-\mathrm{i}\theta}\frac{\partial\psi}{\partial\bar{\kappa}}\right)$$
$$- \frac{\mathrm{i}\,k_x}{k_{\mathrm{S}}}\left(\mathrm{e}^{\mathrm{i}\theta}\frac{\partial\chi}{\partial\kappa} + \mathrm{e}^{-\mathrm{i}\theta}\frac{\partial\chi}{\partial\bar{\kappa}}\right), \tag{B.10}$$

$$u_\theta = \mathrm{i}\left(\mathrm{e}^{\mathrm{i}\theta}\frac{\partial\phi}{\partial\kappa} - \mathrm{e}^{-\mathrm{i}\theta}\frac{\partial\phi}{\partial\bar{\kappa}}\right) - \left(\mathrm{e}^{\mathrm{i}\theta}\frac{\partial\psi}{\partial\kappa} + \mathrm{e}^{-\mathrm{i}\theta}\frac{\partial\psi}{\partial\bar{\kappa}}\right)$$
$$+ \frac{k_x}{k_{\mathrm{S}}}\left(\mathrm{e}^{\mathrm{i}\theta}\frac{\partial\chi}{\partial\kappa} - \mathrm{e}^{-\mathrm{i}\theta}\frac{\partial\chi}{\partial\bar{\kappa}}\right), \tag{B.11}$$

and

$$\sigma_{rr} = -\lambda k_x^2\phi - (\lambda + \mu)\,k_{\mathrm{a}}^2\phi + 2\mu\left(\mathrm{e}^{2\,\mathrm{i}\theta}\frac{\partial^2\phi}{\partial\kappa^2} + \mathrm{e}^{-2\,\mathrm{i}\theta}\frac{\partial^2\phi}{\partial\bar{\kappa}^2}\right)$$
$$+ 2\,\mathrm{i}\,\mu\left(\mathrm{e}^{2\,\mathrm{i}\theta}\frac{\partial^2\psi}{\partial\kappa^2} - \mathrm{e}^{-2\,\mathrm{i}\theta}\frac{\partial^2\psi}{\partial\bar{\kappa}^2}\right) \tag{B.12}$$
$$+ \frac{\mathrm{i}\,\mu k_x k_{\mathrm{b}}^2}{k_{\mathrm{S}}}\chi - \frac{2\,\mathrm{i}\,\mu k_x}{k_{\mathrm{S}}}\left(\mathrm{e}^{2\,\mathrm{i}\theta}\frac{\partial^2\chi}{\partial\kappa^2} + \mathrm{e}^{-2\,\mathrm{i}\theta}\frac{\partial^2\chi}{\partial\bar{\kappa}^2}\right),$$

$$\sigma_{\theta\theta} = -\lambda k_x^2 \phi - (\lambda + \mu)\, k_a^2 \phi - 2\mu \left(e^{2\,i\,\theta} \frac{\partial^2 \phi}{\partial \kappa^2} + e^{-2\,i\,\theta} \frac{\partial^2 \phi}{\partial \bar{\kappa}^2} \right)$$

$$- 2\,i\,\mu \left(e^{2\,i\,\theta} \frac{\partial^2 \psi}{\partial \kappa^2} - e^{-2\,i\,\theta} \frac{\partial^2 \psi}{\partial \bar{\kappa}^2} \right) \tag{B.13}$$

$$+ \frac{i\,\mu k_x k_b^2}{k_S} \chi + \frac{2\,i\,\mu k_x}{k_S} \left(e^{2\,i\,\theta} \frac{\partial^2 \chi}{\partial \kappa^2} + e^{-2\,i\,\theta} \frac{\partial^2 \chi}{\partial \bar{\kappa}^2} \right),$$

$$\sigma_{r\theta} = 2\,i\,\mu \left(e^{2\,i\,\theta} \frac{\partial^2 \phi}{\partial \kappa^2} - e^{-2\,i\,\theta} \frac{\partial^2 \phi}{\partial \bar{\kappa}^2} \right) - 2\mu \left(e^{2\,i\,\theta} \frac{\partial^2 \psi}{\partial \kappa^2} + e^{-2\,i\,\theta} \frac{\partial^2 \psi}{\partial \bar{\kappa}^2} \right)$$

$$+ \frac{2\mu k_x}{k_S} \left(e^{2\,i\,\theta} \frac{\partial^2 \chi}{\partial \kappa^2} - e^{-2\,i\,\theta} \frac{\partial^2 \chi}{\partial \bar{\kappa}^2} \right), \tag{B.14}$$

$$\sigma_{rx} = -2\,i\,\mu k_x \left(e^{i\,\theta} \frac{\partial \phi}{\partial \kappa} + e^{-i\,\theta} \frac{\partial \phi}{\partial \bar{\kappa}} \right) + \mu k_x \left(e^{i\,\theta} \frac{\partial \psi}{\partial \kappa} - e^{-i\,\theta} \frac{\partial \psi}{\partial \bar{\kappa}} \right)$$

$$+ \frac{\mu \left(k_S^2 - 2k_x^2 \right)}{k_S} \left(e^{i\,\theta} \frac{\partial \chi}{\partial \kappa} + e^{-i\,\theta} \frac{\partial \chi}{\partial \bar{\kappa}} \right), \tag{B.15}$$

$$\sigma_{\theta x} = 2\mu k_x \left(e^{i\,\theta} \frac{\partial \phi}{\partial \kappa} - e^{-i\,\theta} \frac{\partial \phi}{\partial \bar{\kappa}} \right) + i\,\mu k_x \left(e^{i\,\theta} \frac{\partial \psi}{\partial \kappa} + e^{-i\,\theta} \frac{\partial \psi}{\partial \bar{\kappa}} \right)$$

$$+ \frac{i\,\mu \left(k_S^2 - 2k_x^2 \right)}{k_S} \left(e^{i\,\theta} \frac{\partial \chi}{\partial \kappa} - e^{-i\,\theta} \frac{\partial \chi}{\partial \bar{\kappa}} \right). \tag{B.16}$$

Appendix C. Derivatives of potentials related to plane and cylindrical waves

Based on the definition of the complex variable $\kappa = y + i\,z$ and its conjugate $\bar{\kappa} = y - i\,z$ given in this paper (i.e., $y = (\kappa + \bar{\kappa})/2$ and $z = -i(\kappa - \bar{\kappa})/2$), the derivative of a function f (which represents a potential related to plane waves) with respect to the complex variables can be calculated using the chain rule:

$$\frac{\partial f}{\partial \kappa} = \frac{\partial y}{\partial \kappa} \frac{\partial f}{\partial y} + \frac{\partial z}{\partial \kappa} \frac{\partial f}{\partial z}, \quad \frac{\partial f}{\partial \bar{\kappa}} = \frac{\partial y}{\partial \bar{\kappa}} \frac{\partial f}{\partial y} + \frac{\partial z}{\partial \bar{\kappa}} \frac{\partial f}{\partial z}. \tag{C.1}$$

The recurrence relation of a Hankel function, for example $H_n^{(2)}(x)$ with the argument x, is given as

$$\frac{2n}{x} H_n^{(2)}(x) = H_{n-1}^{(2)}(x) + H_{n+1}^{(2)}(x). \tag{C.2}$$

The derivative of Hankel functions (which occur in the potentials related to cylindrical waves) with respect to the complex variables (κ and $\bar{\kappa}$) can be derived using the chain rule (see Eq. (C.1)) and the recurrence relation of Hankel functions (see Eq. (C.2)):

$$\frac{\partial}{\partial \kappa} \left[H_n^{(2)} \left(k_a |\kappa + i\,H| \right) \left(\frac{\kappa + i\,H}{|\kappa + i\,H|} \right)^n \right]$$

$$= \frac{k_a}{2} H_{n-1}^{(2)} \left(k_a |\kappa + i\,H| \right) \left(\frac{\kappa + i\,H}{|\kappa + i\,H|} \right)^{n-1}, \tag{C.3}$$

$$\frac{\partial}{\partial \bar{\kappa}} \left[H_n^{(2)} \left(k_a |\kappa + i\,H| \right) \left(\frac{\kappa + i\,H}{|\kappa + i\,H|} \right)^n \right]$$

$$= \frac{-k_a}{2} H_{n+1}^{(2)} \left(k_a |\kappa + i\,H| \right) \left(\frac{\kappa + i\,H}{|\kappa + i\,H|} \right)^{n+1}, \tag{C.4}$$

$$\frac{\partial}{\partial \kappa} \left[H_n^{(2)} \left(k_a |\bar{\kappa} + i\,H| \right) \left(\frac{\bar{\kappa} + i\,H}{|\bar{\kappa} + i\,H|} \right)^n \right]$$

$$= \frac{-k_a}{2} H_{n+1}^{(2)} \left(k_a |\bar{\kappa} + i\,H| \right) \left(\frac{\bar{\kappa} + i\,H}{|\bar{\kappa} + i\,H|} \right)^{n+1}, \tag{C.5}$$

$$\frac{\partial}{\partial \bar{\kappa}} \left[H_n^{(2)} \left(k_a |\bar{\kappa} + i\,H| \right) \left(\frac{\bar{\kappa} + i\,H}{|\bar{\kappa} + i\,H|} \right)^n \right]$$

$$= \frac{k_a}{2} H_{n-1}^{(2)} \left(k_a |\bar{\kappa} + i\,H| \right) \left(\frac{\bar{\kappa} + i\,H}{|\bar{\kappa} + i\,H|} \right)^{n-1}. \tag{C.6}$$

Note that these derivative relationships are also hold for Bessel functions.

Appendix D. Entries of $k_n^{(ji)}$ and $b^{(j)}$ in Eq. (34)

Based on the boundary and continuity conditions (see Eq. (9)), substituting potentials of the total wave fields (see Eqs. (25) and (26)) into the expressions for displacements and stresses in terms of complex variables κ and $\bar{\kappa}$, evaluating the derivative of potentials using Eqs. (C.1) and (C.3)–(C.6), and then replacing the complex variables κ and $\bar{\kappa}$ in the physical domain by complex variables ζ and $\bar{\zeta}$ in the image domain (through appropriate mapping functions, see Eqs. (29) and (30), and their conjugates), we finally obtain Eq. (34), which is a function of complex variables ζ and $\bar{\zeta}$. For the aim of demonstration, this appendix presents the entries of $k_n^{(j,i)}$ and $b^{(j)}$ related to the tenth continuity condition (i.e., $j = 10$, which relates to $\sigma_{r_1\theta_1}^{(1)} = \sigma_{r_1\theta_1}^{(2)}$). For completeness, we also show two terms related to the seventh continuity condition.

The entries of $k_n^{(i,j)}$ related to the tenth continuity condition are written as follows:

$$k_n^{(10,1)} = +\lambda^{(1)} \left(k_x^{(1)} \right)^2 + \left(\lambda^{(1)} + \mu^{(1)} \right) \left(k_a^{(1)} \right)^2 H_n^{(2)} \left(k_a^{(1)} |X_1| \right) \left(\frac{X_1}{|X_1|} \right)^n$$

$$- \frac{\mu^{(1)} \left(k_a^{(1)} \right)^2}{2} \left[e^{2\,i\,\theta} H_{n-2}^{(2)} \left(k_a^{(1)} |X_1| \right) \left(\frac{X_1}{|X_1|} \right)^{n-2} \right.$$

$$\left. + e^{-2\,i\,\theta} H_{n+2}^{(2)} \left(k_a^{(1)} |X_1| \right) \left(\frac{X_1}{|X_1|} \right)^{n+2} \right], \tag{D.1}$$

$$k_n^{(10,2)} = -\frac{i\,\mu^{(1)} \left(k_b^{(1)} \right)^2}{2} \left[e^{2\,i\,\theta} H_{n-2}^{(2)} \left(k_b^{(1)} |X_1| \right) \left(\frac{X_1}{|X_1|} \right)^{n-2} \right.$$

$$\left. - e^{-2\,i\,\theta} H_{n+2}^{(2)} \left(k_b^{(1)} |X_1| \right) \left(\frac{X_1}{|X_1|} \right)^{n+2} \right], \tag{D.2}$$

$$k_n^{(10,3)} = -\frac{i\,\mu^{(1)} k_x^{(1)} \left(k_b^{(1)} \right)^2}{k_S^{(1)}} H_n^{(2)} \left(k_b^{(1)} |X_1| \right) \left(\frac{X_1}{|X_1|} \right)^n$$

$$+ \frac{i\,\mu^{(1)} k_x^{(1)} \left(k_b^{(1)} \right)^2}{2 k_S^{(1)}} \left[e^{2\,i\,\theta} H_{n-2}^{(2)} \left(k_b^{(1)} |X_1| \right) \left(\frac{X_1}{|X_1|} \right)^{n-2} \right. \tag{D.3}$$

$$\left. + e^{-2\,i\,\theta} H_{n+2}^{(2)} \left(k_b^{(1)} |X_1| \right) \left(\frac{X_1}{|X_1|} \right)^{n+2} \right],$$

$$k_n^{(10,4)} = +\lambda^{(1)} \left(k_x^{(1)} \right)^2 + \left(\lambda^{(1)} + \mu^{(1)} \right) \left(k_a^{(1)} \right)^2 H_n^{(2)} \left(k_a^{(1)} |X_2| \right) \left(\frac{X_2}{|X_2|} \right)^n$$

$$- \frac{\mu^{(1)} \left(k_a^{(1)} \right)^2}{2} \left[e^{2\,i\,\theta} H_{n+2}^{(2)} \left(k_a^{(1)} |X_2| \right) \left(\frac{X_2}{|X_2|} \right)^{n+2} \right.$$

$$\left. + e^{-2\,i\,\theta} H_{n-2}^{(2)} \left(k_a^{(1)} |X_2| \right) \left(\frac{X_2}{|X_2|} \right)^{n-2} \right], \tag{D.4}$$

$$k_n^{(10,5)} = -\frac{i\,\mu^{(1)} \left(k_b^{(1)} \right)^2}{2} \left[e^{2\,i\,\theta} H_{n+2}^{(2)} \left(k_b^{(1)} |X_2| \right) \left(\frac{X_2}{|X_2|} \right)^{n+2} \right.$$

$$\left. - e^{-2\,i\,\theta} H_{n-2}^{(2)} \left(k_b^{(1)} |X_2| \right) \left(\frac{X_2}{|X_2|} \right)^{n-2} \right], \tag{D.5}$$

$$k_n^{(10,6)} = -\frac{\mathrm{i}\,\mu^{(1)} k_x^{(1)} \left(k_\mathrm{b}^{(1)}\right)^2}{k_\mathrm{S}^{(1)}} H_n^{(2)}\left(k_\mathrm{b}^{(1)} |X_2|\right) \left(\frac{X_2}{|X_2|}\right)^n$$

$$+ \frac{\mathrm{i}\,\mu^{(1)} k_x^{(1)} \left(k_\mathrm{b}^{(1)}\right)^2}{2 k_\mathrm{S}^{(1)}} \left[\mathrm{e}^{2\mathrm{i}\theta} H_{n+2}^{(2)}\left(k_\mathrm{b}^{(1)} |X_2|\right) \left(\frac{X_2}{|X_2|}\right)^{n+2} \right. \tag{D.6}$$

$$\left. + \mathrm{e}^{-2\mathrm{i}\theta} H_{n-2}^{(2)}\left(k_\mathrm{b}^{(1)} |X_2|\right) \left(\frac{X_2}{|X_2|}\right)^{n-2} \right],$$

$$k_n^{(10,7)} = -\lambda^{(2)}\left(k_x^{(2)}\right)^2 - \left(\lambda^{(2)}+\mu^{(2)}\right)\left(k_\mathrm{a}^{(2)}\right)^2 H_n^{(2)}\left(k_\mathrm{a}^{(2)}|X_3|\right)\left(\frac{X_3}{|X_3|}\right)^n$$

$$+ \frac{\mu^{(2)}\left(k_\mathrm{a}^{(2)}\right)^2}{2}\left[\mathrm{e}^{2\mathrm{i}\theta} H_{n-2}^{(2)}\left(k_\mathrm{a}^{(2)}|X_3|\right)\left(\frac{X_3}{|X_3|}\right)^{n-2}\right.$$

$$\left. + \mathrm{e}^{-2\mathrm{i}\theta} H_{n+2}^{(2)}\left(k_\mathrm{a}^{(2)}|X_3|\right)\left(\frac{X_3}{|X_3|}\right)^{n+2}\right], \tag{D.7}$$

$$k_n^{(10,8)} = +\frac{\mathrm{i}\,\mu^{(2)}\left(k_\mathrm{b}^{(2)}\right)^2}{2}\left[\mathrm{e}^{2\mathrm{i}\theta} H_{n-2}^{(2)}\left(k_\mathrm{b}^{(2)}|X_3|\right)\left(\frac{X_3}{|X_3|}\right)^{n-2}\right.$$

$$\left. - \mathrm{e}^{-2\mathrm{i}\theta} H_{n+2}^{(2)}\left(k_\mathrm{b}^{(2)}|X_3|\right)\left(\frac{X_3}{|X_3|}\right)^{n+2}\right], \tag{D.8}$$

$$k_n^{(10,9)} = +\frac{\mathrm{i}\,\mu^{(2)} k_x^{(2)}\left(k_\mathrm{b}^{(2)}\right)^2}{k_\mathrm{S}^{(2)}} H_n^{(2)}\left(k_\mathrm{b}^{(2)}|X_3|\right)\left(\frac{X_3}{|X_3|}\right)^n$$

$$- \frac{\mathrm{i}\,\mu^{(2)} k_x^{(2)}\left(k_\mathrm{b}^{(2)}\right)^2}{2 k_\mathrm{S}^{(2)}}\left[\mathrm{e}^{2\mathrm{i}\theta} H_{n-2}^{(2)}\left(k_\mathrm{b}^{(2)}|X_3|\right)\left(\frac{X_3}{|X_3|}\right)^{n-2}\right. \tag{D.9}$$

$$\left. + \mathrm{e}^{-2\mathrm{i}\theta} H_{n+2}^{(2)}\left(k_\mathrm{b}^{(2)}|X_3|\right)\left(\frac{X_3}{|X_3|}\right)^{n+2}\right],$$

$$k_n^{(10,10)} = -\lambda^{(2)}\left(k_x^{(2)}\right)^2 - \left(\lambda^{(2)}+\mu^{(2)}\right)\left(k_\mathrm{a}^{(2)}\right)^2 H_n^{(1)}\left(k_\mathrm{a}^{(2)}|X_3|\right)\left(\frac{X_3}{|X_3|}\right)^n$$

$$+ \frac{\mu^{(2)}\left(k_\mathrm{a}^{(2)}\right)^2}{2}\left[\mathrm{e}^{2\mathrm{i}\theta} H_{n-2}^{(1)}\left(k_\mathrm{a}^{(2)}|X_3|\right)\left(\frac{X_3}{|X_3|}\right)^{n-2}\right.$$

$$\left. + \mathrm{e}^{-2\mathrm{i}\theta} H_{n+2}^{(1)}\left(k_\mathrm{a}^{(2)}|X_3|\right)\left(\frac{X_3}{|X_3|}\right)^{n+2}\right], \tag{D.10}$$

$$k_n^{(10,11)} = +\frac{\mathrm{i}\,\mu^{(2)}\left(k_\mathrm{b}^{(2)}\right)^2}{2}\left[\mathrm{e}^{2\mathrm{i}\theta} H_{n-2}^{(1)}\left(k_\mathrm{b}^{(2)}|X_3|\right)\left(\frac{X_3}{|X_3|}\right)^{n-2}\right.$$

$$\left. - \mathrm{e}^{-2\mathrm{i}\theta} H_{n+2}^{(1)}\left(k_\mathrm{b}^{(2)}|X_3|\right)\left(\frac{X_3}{|X_3|}\right)^{n+2}\right], \tag{D.11}$$

$$k_n^{(10,12)} = +\frac{\mathrm{i}\,\mu^{(2)} k_x^{(2)}\left(k_\mathrm{b}^{(2)}\right)^2}{k_\mathrm{S}^{(2)}} H_n^{(1)}\left(k_\mathrm{b}^{(2)}|X_3|\right)\left(\frac{X_3}{|X_3|}\right)^n$$

$$- \frac{\mathrm{i}\,\mu^{(2)} k_x^{(2)}\left(k_\mathrm{b}^{(2)}\right)^2}{2 k_\mathrm{S}^{(2)}}\left[\mathrm{e}^{2\mathrm{i}\theta} H_{n-2}^{(1)}\left(k_\mathrm{b}^{(2)}|X_3|\right)\left(\frac{X_3}{|X_3|}\right)^{n-2}\right. \tag{D.12}$$

$$\left. + \mathrm{e}^{-2\mathrm{i}\theta} H_{n+2}^{(1)}\left(k_\mathrm{b}^{(2)}|X_3|\right)\left(\frac{X_3}{|X_3|}\right)^{n+2}\right],$$

where $X_1 = w^{(1)}\left(\zeta(\beta_\mathrm{o},\vartheta^+)\right) + \mathrm{i}\,H$, $X_2 = \overline{w^{(1)}}\left(\zeta(\beta_\mathrm{o},\vartheta^+)\right) + \mathrm{i}\,H$ and $X_3 = w^{(2)}\left(\zeta(\beta_\mathrm{o},\vartheta)\right) + \mathrm{i}\,H = R_\mathrm{o}$ (considering Eq. (30)). ϑ^+ is a function of ϑ; see Eq. (33). The terms of $\mathrm{e}^{+2\mathrm{i}\theta}$ and $\mathrm{e}^{-2\mathrm{i}\theta}$ in the first six entries (i.e., $k_n^{(10,1)} - k_n^{(10,6)}$) and in the last six entries (i.e., $k_n^{(10,7)} - k_n^{(10,12)}$), respectively are written as functions of variable ϑ in the image domain

as follows:

$$\mathrm{e}^{2\mathrm{i}\theta} = \mathrm{e}^{2\mathrm{i}\vartheta^+}\left[\frac{w^{(1)'}(\zeta)}{|w^{(1)'}(\zeta)|}\right]^2 = -\left(\frac{\mathrm{e}^{\mathrm{i}\,\vartheta^+}-\beta_\mathrm{o}}{1-\beta_\mathrm{o}\mathrm{e}^{\mathrm{i}\,\vartheta^+}}\right)^2,$$

$$\mathrm{e}^{-2\mathrm{i}\theta} = -\left(\frac{1-\beta_\mathrm{o}\mathrm{e}^{\mathrm{i}\,\vartheta^+}}{\mathrm{e}^{\mathrm{i}\,\vartheta^+}-\beta_\mathrm{o}}\right)^2, \tag{D.13}$$

$$\mathrm{e}^{2\mathrm{i}\theta} = \mathrm{e}^{2\mathrm{i}\vartheta}, \quad \mathrm{e}^{-2\mathrm{i}\theta} = \mathrm{e}^{-2\mathrm{i}\vartheta}. \tag{D.14}$$

Similarly, the terms of $\mathrm{e}^{\mathrm{i}\theta}$ and $\mathrm{e}^{-\mathrm{i}\theta}$ in the first six entries, for example, in the seventh continuity condition, (i.e., $k_n^{(7,1)} - k_n^{(7,6)}$) and in the last six entries (i.e., $k_n^{(7,7)} - k_n^{(7,12)}$), respectively are written as functions of variable ϑ in the image domain as follows:

$$\mathrm{e}^{\mathrm{i}\theta} = \mathrm{e}^{\mathrm{i}\,\vartheta^+}\frac{w^{(1)'}(\zeta)}{|w^{(1)'}(\zeta)|} = \left|\frac{\left(1-\beta_\mathrm{o}\mathrm{e}^{\mathrm{i}\,\vartheta^+}\right)^2}{2\,\mathrm{i}\,G}\right|\frac{-2\,\mathrm{i}\,G\mathrm{e}^{\mathrm{i}\,\vartheta^+}}{\left(1-\beta_\mathrm{o}\mathrm{e}^{\mathrm{i}\,\vartheta^+}\right)^2},$$

$$\mathrm{e}^{-\mathrm{i}\theta} = \left|\frac{\left(1-\beta_\mathrm{o}\mathrm{e}^{\mathrm{i}\,\vartheta^+}\right)^2}{2\,\mathrm{i}\,G}\right|\frac{2\,\mathrm{i}\,G\mathrm{e}^{\mathrm{i}\,\vartheta^+}}{\left(\mathrm{e}^{\mathrm{i}\,\vartheta^+}-\beta_\mathrm{o}\right)^2}, \tag{D.15}$$

$$\mathrm{e}^{\mathrm{i}\theta} = \mathrm{e}^{\mathrm{i}\,\vartheta}, \quad \mathrm{e}^{-\mathrm{i}\theta} = \mathrm{e}^{-\mathrm{i}\,\vartheta}. \tag{D.16}$$

The entry of $b^{(j)}$ related to the tenth continuity condition, with the incident P wave ($\phi_\mathrm{inc}^{(1)}$) taken as an example, reads as follows:

$$b^{(10)} = -\lambda^{(1)}\left(k_x^{(1)}\right)^2 - \left(\lambda^{(1)}+\mu^{(1)}\right)\left(\phi_\mathrm{inc}^{(1)}+\phi_\mathrm{ref}^{(1)}\right)$$

$$+ 2\,\mathrm{i}\,\mu^{(1)}\left[\mathrm{e}^{2\mathrm{i}\theta}\left(-\frac{\mathrm{i}\,k_y^{(1)}-k_{z,\mathrm{S}}^{(1)}}{2}\right)^2 - \mathrm{e}^{-2\mathrm{i}\theta}\left(-\frac{\mathrm{i}\,k_y^{(1)}+k_{z,\mathrm{S}}^{(1)}}{2}\right)^2\right]\psi_\mathrm{ref}^{(1)}$$

$$+ 2\mu^{(1)}\left\{\left[\mathrm{e}^{2\mathrm{i}\theta}\left(-\frac{\mathrm{i}\,k_y^{(1)}+k_{z,\mathrm{P}}^{(1)}}{2}\right)^2 + \mathrm{e}^{-2\mathrm{i}\theta}\left(-\frac{\mathrm{i}\,k_y^{(1)}-k_{z,\mathrm{P}}^{(1)}}{2}\right)^2\right]\phi_\mathrm{inc}^{(1)}\right.$$

$$\left. + \left[\mathrm{e}^{2\mathrm{i}\theta}\left(-\frac{\mathrm{i}\,k_y^{(1)}-k_{z,\mathrm{P}}^{(1)}}{2}\right)^2 + \mathrm{e}^{-2\mathrm{i}\theta}\left(-\frac{\mathrm{i}\,k_y^{(1)}+k_{z,\mathrm{P}}^{(1)}}{2}\right)^2\right]\phi_\mathrm{ref}^{(1)}\right\}$$

$$+ \frac{\mathrm{i}\,\mu^{(1)} k_x^{(1)}\left(k_\mathrm{b}^{(1)}\right)^2}{k_\mathrm{S}^{(1)}}\chi_\mathrm{ref}^{(1)} - \frac{2\,\mathrm{i}\,\mu^{(1)} k_x^{(1)}\left(k_\mathrm{b}^{(1)}\right)^2}{k_\mathrm{S}^{(1)}}\left[\mathrm{e}^{2\mathrm{i}\theta}\left(-\frac{\mathrm{i}\,k_y^{(1)}-k_{z,\mathrm{S}}^{(1)}}{2}\right)^2\right.$$

$$\left. + \mathrm{e}^{-2\mathrm{i}\theta}\left(-\frac{\mathrm{i}\,k_y^{(1)}+k_{z,\mathrm{S}}^{(1)}}{2}\right)^2\right]\chi_\mathrm{ref}^{(1)}, \tag{D.17}$$

where the terms of $\mathrm{e}^{+2\mathrm{i}\theta}$ and $\mathrm{e}^{-2\mathrm{i}\theta}$ have the expressions as shown in Eq. (D.13), and

$$\phi_\mathrm{inc}^{(1)} = \phi_0 \exp\left(-\mathrm{i}\,k_x^{(1)}x\right)\exp\left[\left(-\frac{\mathrm{i}\,k_y^{(1)}+k_{z,\mathrm{P}}^{(1)}}{2}\right)w^{(1)}\left(\zeta(\beta_\mathrm{o},\vartheta^+)\right)\right.$$

$$\left. + \left(-\frac{\mathrm{i}\,k_y^{(1)}-k_{z,\mathrm{P}}^{(1)}}{2}\right)\overline{w^{(1)}}\left(\zeta(\beta_\mathrm{o},\vartheta^+)\right)\right], \tag{D.18}$$

$$\phi_\mathrm{ref}^{(1)} = R_{\phi,\phi}\phi_0 \exp\left(-\mathrm{i}\,k_x^{(1)}x\right)\exp\left[\left(-\frac{\mathrm{i}\,k_y^{(1)}-k_{z,\mathrm{P}}^{(1)}}{2}\right)w^{(1)}\left(\zeta(\beta_\mathrm{o},\vartheta^+)\right)\right.$$

$$\left. + \left(-\frac{\mathrm{i}\,k_y^{(1)}+k_{z,\mathrm{P}}^{(1)}}{2}\right)\overline{w^{(1)}}\left(\zeta(\beta_\mathrm{o},\vartheta^+)\right)\right], \tag{D.19}$$

$$\psi_\mathrm{ref}^{(1)} = R_{\psi,\phi}\phi_0 \exp\left(-\mathrm{i}\,k_x^{(1)}x\right)\exp\left[\left(-\frac{\mathrm{i}\,k_y^{(1)}-k_{z,\mathrm{S}}^{(1)}}{2}\right)w^{(1)}\left(\zeta(\beta_\mathrm{o},\vartheta^+)\right)\right.$$

$$+ \left(-\frac{\mathrm{i}\, k_y^{(1)} + k_{z,\mathrm{S}}^{(1)}}{2} \right) \overline{w^{(1)}} \left(\zeta(\beta_{\mathrm{o}}, \vartheta^+) \right) \Bigg], \tag{D.20}$$

$$\chi_{\mathrm{ref}}^{(1)} = R_{\chi,\phi} \phi_0 \exp\left(-\mathrm{i}\, k_x^{(1)} x \right) \exp\left[\left[\left(-\frac{\mathrm{i}\, k_y^{(1)} - k_{z,\mathrm{S}}^{(1)}}{2} \right) w^{(1)} \left(\zeta(\beta_{\mathrm{o}}, \vartheta^+) \right) \right. \right.$$

$$+ \left(-\frac{\mathrm{i}\, k_y^{(1)} + k_{z,\mathrm{S}}^{(1)}}{2} \right) \overline{w^{(1)}} \left(\zeta(\beta_{\mathrm{o}}, \vartheta^+) \right) \Bigg]. \tag{D.21}$$

References

[1] Mow CC, Pao YH. The diffraction of elastic waves and dynamic stress concentrations. New York: Crane-Russak; 1971.

[2] Achenbach JD. Wave propagation in elastic solids. Amsterdam: Nord-Holland-Elsevier; 1973.

[3] Aki K, Richards PG. Quantitative seismology. University Science Books; 2002.

[4] Graff KF. Wave motion in elastic solids. Ohio State University Press; 1975.

[5] Stamos AA, Beskos DE. Dynamic analysis of large 3-D underground structures by the BEM. Earthq Eng Struct Dyn 1995;24(6):917–34.

[6] Luco JE, De Barros FCP. Seismic response of a cylindrical shell embedded in a layered viscoelastic half-space. I: Formulation. Earthq Eng Struct Dyn 1994;23(5):553–67.

[7] Luco JE, De Barros FCP. Dynamic displacements and stresses in the vicinity of a cylindrical cavity embedded in a half-space. Earthq Eng Struct Dyn 1994;23(3):321–40.

[8] De Barros FCP, Luco JE. Diffraction of obliquely incident waves by a cylindrical cavity embedded in a layered viscoelastic half-space. Soil Dyn Earthq Eng 1993;12(3):159–71.

[9] Luco JE, De Barros FCP. On the three-dimensional seismic response of a class of cylindrical inclusions embedded in layered media. In: International conference on soil dynamics and earthquake engineering. 1993, p. 565–80.

[10] De Barros FCP, Luco JE. Seismic response of a cylindrical shell embedded in a layered viscoelastic half-space. II: Validation and numerical results. Earthq Eng Struct Dyn 1994;23(5):569–80.

[11] Dravinski M, Mossessian TK. Scattering of plane harmonic P, SV, and Rayleigh waves by dipping layers of arbitrary shape. Bull Seismol Soc Am 1987;77(1):212–35.

[12] Stamos AA, Beskos DE. 3-D seismic response analysis of long lined tunnels in half-space. Soil Dyn Earthq Eng 1996;15(2):111–8.

[13] Liu SW, Datta SK, Khair KR, Shah AH. Three dimensional dynamics of pipelines buried in backfilled trenches due to oblique incidence of body waves. Soil Dyn Earthq Eng 1991;10(4):182–91.

[14] Israil ASM, Banerjee PK. Two-dimensional transient wave-propagation problems by time-domain BEM. Int J Solids Struct 1990;26(8):851–64.

[15] Hatzigeorgiou GD, Beskos DE. Soil–structure interaction effects on seismic inelastic analysis of 3-D tunnels. Soil Dyn Earthq Eng 2010;30(9):851–61.

[16] Alielahi H, Kamalian M, Adampira M. Seismic ground amplification by unlined tunnels subjected to vertically propagating SV and P waves using BEM. Soil Dyn Earthq Eng 2015;71:63–79.

[17] Alielahi H, Kamalian M, Adampira M. A BEM investigation on the influence of underground cavities on the seismic response of canyons. Acta Geotech 2016;11(2):391–413.

[18] Panji M, Ansari B. Transient SH-wave scattering by the lined tunnels embedded in an elastic half-plane. Eng Anal Bound Elem 2017;84:220–30.

[19] Balendra T, Thambiratnam DP, Koh CG, Lee S-L. Dynamic response of twin circular tunnels due to incident SH-waves. Earthq Eng Struct Dyn 1984;12(2):181–201.

[20] Datta SK, El-Akily N. Diffraction of elastic waves by cylindrical cavity in a half-space. J Acoust Soc Am 1978;64(6):1692–9.

[21] El-Akily N, Datta SK. Response of a circular cylindrical shell to disturbances in a half-space. Earthq Eng Struct Dyn 1980;8(5):469–77.

[22] El-Akily N, Datta SK. Response of a circular cylindrical shell to disturbances in a half-space - numerical results. Earthq Eng Struct Dyn 1981;9(5):477–87.

[23] Lee VW, Zhu G. A note on three-dimensional scattering and diffraction by a hemispherical canyon–I: Vertically incident plane P-wave. Soil Dyn Earthq Eng 2014;61–62:197–211.

[24] Wong KC, Datta SK, Shah AH. Three-dimensional motion of buried pipeline. I: Analysis. J Eng Mech 1986;112(12):1319–37.

[25] Wong KC, Shah AH, Datta SK. Three-dimensional motion of buried pipeline. II: Numerical results. J Eng Mech 1986;112(12):1338–45.

[26] Cao H, Lee VW. Scattering and diffraction of plane p waves by circular cylindrical canyons with variable depth-to-width ratio. Soil Dyn Earthq Eng 1990;9(3):141–50.

[27] Lee VW, Karl J. Diffraction of SV waves by underground, circular, cylindrical cavities. Soil Dyn Earthq Eng 1992;11(8):445–56.

[28] Muskhelishvili N. Some basic problems of the mathematical theory of elasticity. Moscow: Nauka; 1966.

[29] Liu D, Gai B, Tao G. Applications of the method of complex functions to dynamic stress concentrations. Wave Motion 1982;4(3):293–304.

[30] Verruijt A. Deformations of an elastic half plane with a circular cavity. Int J Solids Struct 1998;35(21):2795–804.

[31] Liu Q, Wang R. Dynamic response of twin closely-spaced circular tunnels to harmonic plane waves in a full space. Tunnel Undergr Space Technol 2012;32:212–20.

[32] Liu Q, Zhao M, Wang L. Scattering of plane P, SV or Rayleigh waves by a shallow lined tunnel in an elastic half space. Soil Dyn Earthq Eng 2013;49:52–63.

[33] Kausel E. Fundamental solutions in elastodynamics: a compendium. Cambridge University Press; 2006.

[34] Lee VW, Trifunac MD. Response of tunnels to incident SH-waves. J Eng Mech Div 1979;105(4):643–59.

[35] Datta SK, Shah AH, Wong KC. Dynamic stresses and displacements in buried pipe. J Eng Mech 1984;110(10):1451–66.

[36] Zhao M, de Oliveira Barbosa JM, Yuan J, Metrikine AV, van Dalen KN. Instability of vibrations of an oscillator moving at high speed through a tunnel embedded in soft soil. J Sound Vib 2021;494:115776.